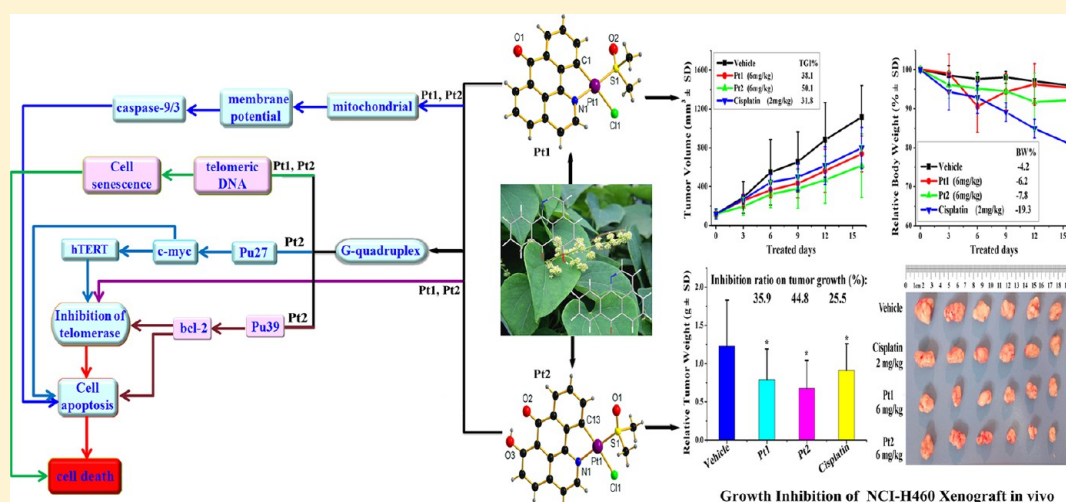


Stabilization of G-Quadruplex DNA, Inhibition of Telomerase Activity, and Tumor Cell Apoptosis by Organoplatinum(II) Complexes with Oxoisoaporphine

Zhen-Feng Chen,* Qi-Pin Qin, Jiao-Lan Qin, Yan-Cheng Liu, Ke-Bin Huang, Yu-Lan Li, Ting Meng, Guo-Hai Zhang, Yan Peng, Xu-Jian Luo, and Hong Liang*

State Key Laboratory Cultivation Base for the Chemistry and Molecular Engineering of Medicinal Resources, School of Chemistry and Pharmacy, Guangxi Normal University, Yucai Road 15, Guilin 541004, P. R. China

S Supporting Information



ABSTRACT: Two G-quadruplex ligands [Pt(L^a)(DMSO)Cl] (Pt1) and [Pt(L^b)(DMSO)Cl] (Pt2) have been synthesized and fully characterized. The two complexes are more selective for SK-OV-3/DDP tumor cells versus normal cells (HL-7702). It was found that both Pt1 and Pt2 could be a telomerase inhibitor targeting G-quadruplex DNA. This is the first report demonstrating that telomeric, c-myc, and bcl-2 G-quadruplexes and caspase-3/9 preferred to bind with Pt2 rather than Pt1, which also can induce senescence and apoptosis. The different biological behavior of Pt1 and Pt2 may correlate with the presence of a 6-hydroxyl group in L^b. Importantly, Pt1 and Pt2 exhibited higher safety in vivo and more effective inhibitory effects on tumor growth in the HCT-8 and NCI-H460 xenograft mouse model, compared with cisplatin. Taken together, these mechanistic insights indicate that both Pt1 and Pt2 display low toxicity and could be novel anticancer drug candidates.

INTRODUCTION

Telomere structures contain highly repetitive guanine (G) rich DNA sequences and are essential for maintaining the stability of eukaryotic chromosomes. Human telomeric DNA is composed of a repeated double-stranded [TTAGGG-CCCTAA]_n sequence except for the 3'-terminal region, which consists of a single-stranded tandem [TTAGGG] repeated sequence over several hundred bases.¹ Recent studies demonstrate that G-quadruplex structures are stable and detectable in human cells.² G-quadruplexes participate in several key biological events, especially those associated with aging and diseases. They are involved in the regulation of telomerase activity that is activated in 80–90% of human tumors and can serve as specific tumor-selective targets for chemotherapy.^{3–6}

In addition, the G-quadruplex structure has recently been found not only in telomeres but also in promoter regions of certain genes such as c-myc, bcl-2, and c-kit, and these G-quadruplexes have their own specific structures.⁷ The formation or stabilization of G-quadruplexes in these regions may play a key regulatory role. In c-myc oncogene, G-rich sequences can form c-myc G-quadruplexes and regulate the transcription of c-myc oncogene. The c-myc functions as a gene-specific transcription factor through its protein product that controls a variety of genes responsible for a wide range of human cancers.⁸ Particular interest has been focused on c-myc, another important quadrome gene involved in cell senescence,⁹ transcriptionally activating the catalytic subunit of telomerase

Received: August 14, 2014

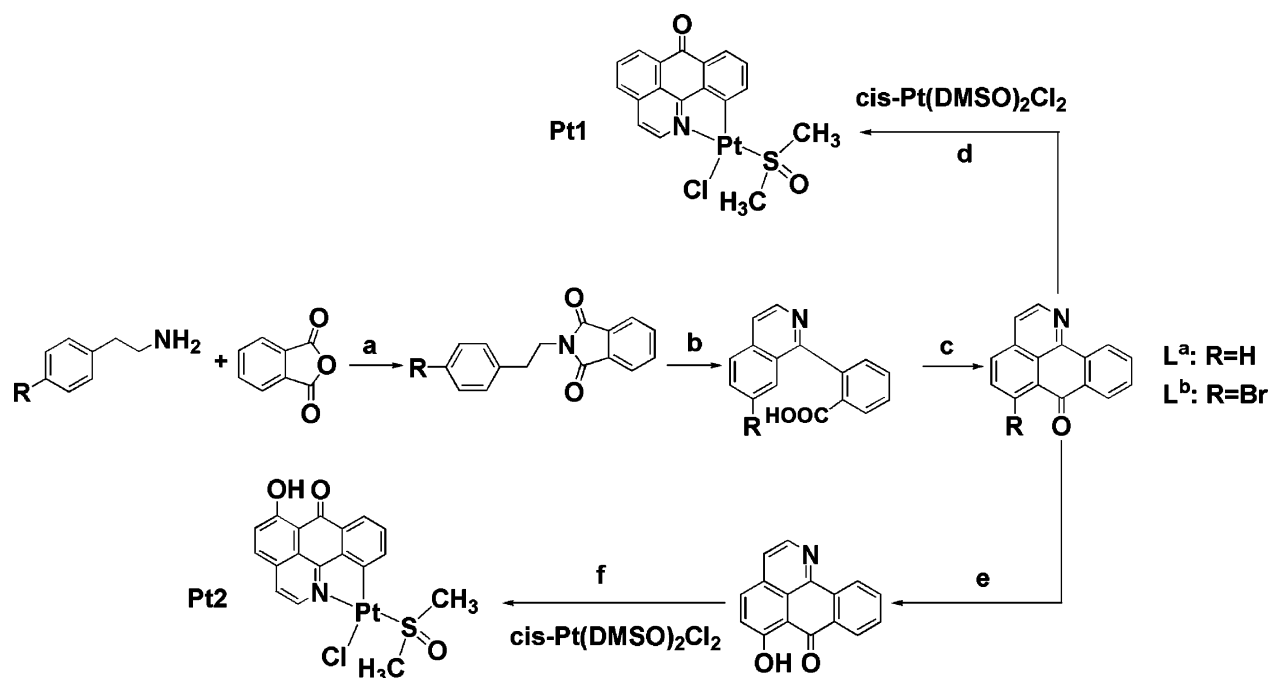


Figure 1. Synthetic routes for the preparation of the 1-azabenzanthrone (L^a), 6-hydroxyoxoisoaporphine alkaloid (L^b), and their platinum(II) complexes Pt1 and Pt2. Reagents are the following: (a) ethanol (reflux); (b) anhydrous $AlCl_3/NaCl$ (220–230 °C); (c) concentrated H_2SO_4 (230–240 °C); (d) ethanol/water (10:1) (reflux); (e) NaOH (room temperature 24 h); (f) methanol/water (25:1) (reflux).

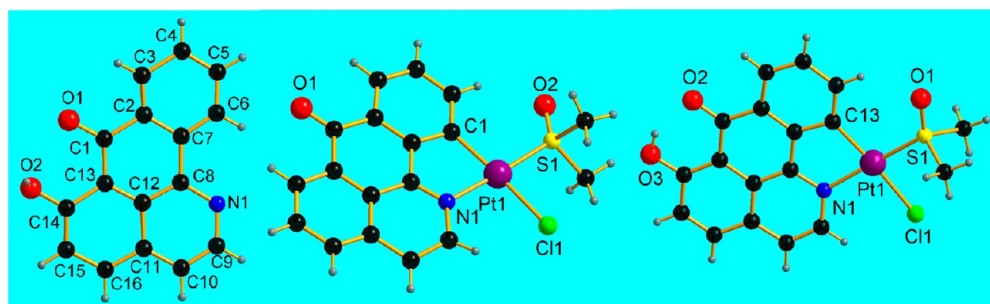


Figure 2. Crystal structures of L^b (left) and Pt1 (middle) and Pt2 (right) showing atom labeling.

hTERT¹⁰ and consequently influencing the elongation of telomere. Another apoptosis-related human bcl-2 oncogene also contains a GC-rich sequence which is located upstream from P1 promoter and has the potential to form G-quadruplex structures¹¹ and regulate the transcription of bcl-2. Therefore, targeting G-quadruplexes in gene promoters may constitute a novel anticancer strategy.¹²

During the past decade, a number of small molecules have been reported to efficiently stabilize G-quadruplex DNA, inhibit the telomerase activity, or regulate the gene expression.^{11,13} Most of these compounds are organic compounds with a large planar aromatic conjugated system, which in general can stabilize the G-quadruplex structure mainly by π - π stacking and electrostatic interactions with G-quartet plane of G-quadruplex DNA.¹⁴ Some G-quadruplex binders that are capable of binding to the groove and loop have also been reported recently.¹⁵ On the other hand, metal complexes have a very broad range of structural and electronic properties that can be successfully exploited when designing quadruplex DNA binders. Furthermore, the metal complexes possess interesting optical, magnetic, or catalytic properties and could in principle be exploited for the development of quadruplex probes and

cleaving agents. Similar to organic compounds, they can stabilize the G-quadruplex via π - π stacking and electrostatic interactions and have the ability to interact with nucleic acids (including quadruplex DNA) through alternative and/or additional modes, such as direct coordination to bases or the phosphate backbone.¹⁶ Because of the great potential of the metal complexes as G-quadruplex binders, more and more metal complex G-quadruplex DNA binders have been reported recently, such as nickel(II),¹⁷ platinum(II),^{18,19} palladium(II),²⁰ ruthenium(II),²¹ copper(II),²² cobalt(II), and zinc(II).²³ Among them, the platinum(II) complex G-quadruplex binders are most widely exploited for their great potential as anticancer agents.¹⁸ Therefore, we synthesized two organoplatinum(II) complexes with structures as depicted in Figures 1 and 2 and investigated their abilities to act as selective and effective G-quadruplex binders. The rationale is to maintain the planar π -conjugation of the 1-azabenzanthrone or 6-hydroxyoxoisoaporphine alkaloid scaffolds through the formation of platinum(II) complexes, which have a more extended π -conjugated planar aromatic structure. This approach can significantly improve their π - π interactions with G-quadruplex and can also covalently bind to guanine of G-quadruplex. These

Table 1. IC₅₀ (μM) Values of L^a, L^b, Pt1, and Pt2 for the Selected Cells for 48 h

compd	T-24	Hep-G2	SK-OV-3	SK-OV-3/DDP	BEL-7404	NCI-H460	HCT-8	HL-7702
L ^a	16.8 ± 2.0	17.4 ± 4.6	>100	36.8 ± 1.5	36.7 ± 0.1	>100	>100	>100
L ^b	38.4 ± 1.5	20.5 ± 1.3	>100	13.9 ± 2.2	54.7 ± 0.2	66.9 ± 0.5	60.2 ± 0.7	64.5 ± 0.4
1	4.8 ± 1.7	14.3 ± 1.6	37.6 ± 3.6	4.8 ± 0.9	15.6 ± 0.3	38.4 ± 0.9	36.5 ± 0.4	>100
2	26.7 ± 1.9	14.4 ± 2.0	30.5 ± 2.4	4.5 ± 0.4	26.2 ± 0.8	10.7 ± 0.6	13.2 ± 0.5	>100
cisplatin ^a	28.1 ± 0.7	9.5 ± 0.4	15.6 ± 1.7	65.9 ± 1.5	12.4 ± 0.4	18.9 ± 0.5	15.4 ± 0.6	15.6 ± 0.3

^aCisplatin is the clinical medicine.

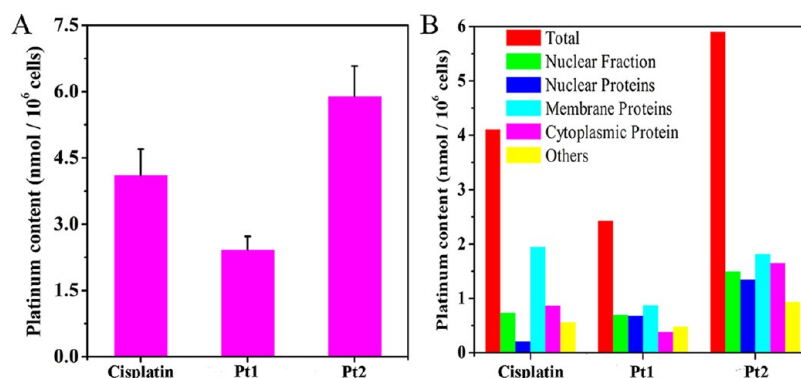


Figure 3. SK-OV-3/DDP cells were treated with Pt1 and Pt2 for 8 h at 37 °C. Platinum content in whole cell (A) and in different fraction (B) was measured by ICP-MS. Control cells were treated with vehicle (1% DMSO). Data shown are mean values ± standard deviations of three independent measurements for each experiment.

compounds can induce tumor cell apoptosis through multiple mechanisms, especially in cisplatin-resistant tumor cells SK-OV-3/DDP. Meanwhile, using cisplatin as positive control, we further investigated the in vivo antitumor efficacy of Pt1 and Pt2 utilizing HCT-8 and NCI-H460 xenograft models.

RESULTS AND DISCUSSION

Synthesis and Characterization. The ligands 1-azabenzanthrone (L^a) and 6-hydroxyloxoisoaporphine alkaloid (L^b) were synthesized according to the reported procedures (Figure 1).²⁴ Their structures were characterized by IR, ESI-MS, ¹H and ¹³C NMR spectrometry, and elemental analyses. In addition, L^b was structurally characterized by single-crystal X-ray diffraction analysis. Its crystal structure is shown in Figure 2. Selected bond lengths (Å) and bond angles (deg) for L^b are reported in Table S1 (Supporting Information), and crystal data and structure refinement parameters for L^b are listed Table S2 (Supporting Information). As shown in Figure 2, L^b has a planar structure similar to 10-chloro-1-azabenzanthrone.²⁵

Crystal Structures of Pt1 and Pt2. Pt1 and Pt2 were prepared via the reaction of cis-Pt(DMSO)₂Cl₂ with L^a and L^b in the presence of ethanol (or methanol) and water under solvothermal conditions (Figure 1). Their structures were characterized by IR, ¹H and ¹³C NMR, ESI-MS (Supporting Information, Figures S1–S17), and elemental analysis. The single-crystal X-ray diffraction analyses for Pt1 and Pt2 revealed that in each case the platinum(II) center is four coordinated by the corresponding chelating ligand (C^N-L^a or C^N-L^b) via the heterocyclic nitrogen and carbon atom, one DMSO ligand via the sulfur atom, and one chlorine, to form a square-planar geometry (Figure 2). Selected bond lengths (Å) and bond angles (deg) are reported in Table S1 (Supporting Information), and crystal data and structure refinement parameters are listed Table S2 (Supporting Information). Because L^b contains a 6-hydroxyl group and different from L^a,

Pt2 may lead to an increase in the membrane permeability and the affinity to the molecular targets, which is responsible for its high cytotoxicity.

Stability of Pt1 and Pt2 in Solution. L^a, L^b, Pt1, and Pt2 were tested for their stability in physiological conditions (Tris-KCl buffer solution with pH value of 7.35, containing 1% DMSO) by means of UV-vis spectroscopy. As shown in Figure S18 (Supporting Information), the time-dependent (at 0, 2, 4, 8, 12, and 24 h) UV-vis spectra of each compound indicated that L^a, L^b, Pt1, and Pt2 were stable in TBS (Tris buffer solution) for 24 h at room temperature. Their stabilities were further confirmed by HPLC experiments. As shown in Figure S19 (Supporting Information), all four molecules were stable for 24 h in DMSO stock solution.

In Vitro Cytotoxicity. The in vitro cytotoxicity of L^a and L^b and their platinum complexes Pt1 and Pt2 (cisplatin as positive control) against seven human tumor cells T-24, Hep-G2, SK-OV-3, SK-OV-3/DDP, BEL-7404, NCI-H460, and HCT-8 and one normal liver cell HL-7702 was assessed by MTT assay. The inhibitory rates are listed in Table S3 (Supporting Information). For comparison, cisplatin and Pt(DMSO)₂Cl₂ were used as controls. After incubation of the cells with the compounds at a concentration of 20 μM for 48 h under identical conditions, these compounds exhibited different antitumor activity and certain extent of selectivity. Against the tested tumor cells, the inhibitory rates of Pt1 and Pt2 were higher than that of L^a, L^b, and Pt(DMSO)₂Cl₂, respectively. Interestingly, L^a, L^b, Pt1, and Pt2 displayed low inhibitory rates against normal live cell HL-7702. The in vitro antitumor activities of Pt1 and Pt2 were further quantified by determining the corresponding IC₅₀ values. As shown in Table 1, Pt1 and Pt2 exhibited significantly enhanced cytotoxicity compared with free L^a and L^b in general. For example, Pt1 was 2.5 times stronger than L^a against T-24, and Pt1 and Pt2 were more cytotoxic to SK-OV-3/DDP cisplatin-resistant tumor cells than to SK-OV-3. They showed low IC₅₀ values (4.5–4.8 μM) on SK-OV-3/DDP, more than

2.5–7 times more cytotoxic than the corresponding free L^a and L^b , and even 13 times more cytotoxic than cisplatin alone. Pt2 was more toxic than Pt1 and cisplatin toward NCI-H460 and HCT-8. According to Table S3 (Supporting Information) and Table 1, Pt1 and Pt2 displayed a synergistic effect upon the combination of platinum with corresponding oxoisoaporphine alkaloids L^a and L^b .

Cellular Uptake and Distribution of Platinum in Cancer Cells. Since Pt1 and Pt2 exhibited the best in vitro cytotoxicity on SK-OV-3/DDP cells, we selected these cells to investigate the cellular uptake and distribution of platinum in cancer cells, using the inductively coupled plasma mass spectrometry. Treating SK-OV-3/DDP cells with the complexes ($10.0 \mu\text{M}$) for 8 h resulted in a substantial increase in the cellular platinum concentration compared to the untreated control, suggesting facile internalization of complexes within 8 h. As shown in Figure 3A, Pt2 ($(5.90 \pm 0.68 \text{ nmol of Pt})/10^6 \text{ cells}$) was taken up by the cells approximately 2.44 times and 1.5 times more efficiently than Pt1 ($(2.42 \pm 0.30 \text{ nmol of Pt})/10^6 \text{ cells}$) and cisplatin ($(4.11 \pm 0.59 \text{ nmol of Pt})/10^6 \text{ cells}$), respectively.

To examine the cellular distributions of Pt1 and Pt2, the platinum concentrations were determined in the nuclear fraction, nuclear proteins, membrane proteins, cytoplasmic protein, and other extracts fractionated from SK-OV-3/DDP cells after the exposure of the cells to Pt1 and Pt2 for 8 h according to the reported method.²⁶ As shown in Figure 3B, Pt1 and Pt2 all accumulated to a high extent in the nuclear fraction and membrane fraction, while cisplatin only accumulated in the membrane fraction. The percentage of platinum from Pt2 in the nuclear fraction was slightly higher than that from Pt1 and cisplatin. It is also notable that there was a certain amount of accumulation of platinum from the complexes in the other fractions, including the total soluble proteins. The differences in cellular platinum distribution can be attributed to the different cellular pathways involved in the uptake and efflux of the platinum complexes, which may be related to the apoptotic pathways they activated.

Confocal Microscopy Examination. The AO/EB molecular probes were used to detect apoptotic cells.²⁷ As shown in Figure 4, apparent changes of cell morphology took place after treating the SK-OV-3/DDP tumor cells with $5.0 \mu\text{M}$ Pt1 and Pt2 for 12 h. Pt1 caused a small number of SK-OV-3/DDP cells to shrink and undergo apoptosis. In contrast, Pt2 caused a large number of SK-OV-3/DDP cells to shrink and undergo apoptosis. The apoptotic body was observed obviously. The results primarily suggested that both Pt1 and Pt2 could induce apoptosis in SK-OV-3/DDP cells at $5.0 \mu\text{M}$ dosage after 12 h of treatment. However, Pt2 exhibited stronger ability to induce apoptosis than Pt1, which might be attributed to the 6-hydroxyl group in the L^b of Pt2.

The ability of Pt1 and Pt2 to induce apoptosis was further confirmed by analyzing the nuclear morphology of the compound-treated SK-OV-3/DDP tumor cells. SK-OV-3/DDP tumor cells were treated with Pt1 and Pt2 for 12 h and stained with membrane-permeable blue Hoechst 33258 to detect apoptosis morphologically. As shown in Figure 5, the Hoechst 33258 fluorescent photomicrographs of cultured SK-OV-3/DDP tumor cells treated with 5.0 , 10.0 , and $20.0 \mu\text{M}$ Pt1 and Pt2 for 12 h, respectively, indicated that in the control cultures, nuclei of SK-OV-3/DDP tumor cells appeared with regular contours and were round, and SK-OV-3/DDP tumor cells with smaller nuclei and condensed chromatin were rarely

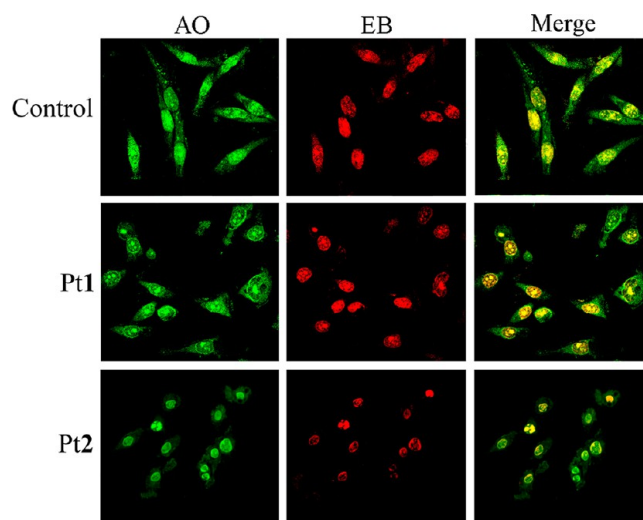


Figure 4. Confocal microscopy of the SK-OV-3/DDP cells treated with $5.0 \mu\text{M}$ Pt1, Pt2 for 12 h. Images were acquired using a CarlZeiss LSM 710 microscope (magnification $400\times$).

seen. Treatment with $5.0 \mu\text{M}$ Pt1 slightly changed the nuclear morphology (Figure 5B), and more nuclei of Pt1-treated SK-OV-3/DDP tumor cells appeared hypercondensed (brightly stained) at $10.0 \mu\text{M}$ (Figure 5C). It should be noted that the numbers of apoptotic nuclei containing condensed chromatin increased significantly as the result of treatment with $20.0 \mu\text{M}$ Pt1 (Figure 5D). Similar results were observed with Pt2 treatment, but it was interesting to find that treatment with $5.0 \mu\text{M}$ Pt2 induced significant apoptosis (Figure 5F). With the increased concentrations of Pt2, the number of apoptotic nuclei increased more significantly than treatment with Pt1.

Senescence Induction. To evaluate the long-term effects of Pt1 and Pt2 on SK-OV-3/DDP cancer cells, subcytotoxic concentrations ($0.5 \mu\text{M}$) of both compounds were employed to avoid acute cytotoxicity and other nonspecific events that could lead to difficulty in interpretation of results. Seven days after treatment with $0.5 \mu\text{M}$ Pt1 and Pt2, SK-OV-3/DDP cells displayed increased proportion of flat and giant cells with phenotypic characteristics of senescence as revealed by the senescence-associated β -galactosidase (SA- β -Gal) assay (Figure 6).²⁸ The results indicated that Pt2 might induce senescence mainly due to the shortening of telomere length, whereas the effect of Pt1 on SK-OV-3/DDP cells was not so obvious, implying that dysfunctional telomeres could initiate cellular senescence or apoptosis to suppress tumorigenesis.

Cell Cycle and Apoptosis. In order to confirm the cell morphological analytical results, we further investigated the cell cycle and apoptosis using SK-OV-3/DDP tumor cells. The cell cycle analysis of untreated and treated SK-OV-3/DDP cells for 48 h with $5.0 \mu\text{M}$ Pt1 and Pt2 showed that both compounds induced evident perturbation of the cell cycle and blocked the cells in G2 and G1 phases, respectively (Figure 7 and Figure S20, Supporting Information). G2 population of 36.24% was observed in Pt1 group, while the corresponding G2 population of 8.23% was observed in untreated control cells, which was different from the cycle G1 arrest in Pt2-treated cells, where the G1 population was 70.07%, compared with a G1 population of 51.81% in the control group.

We further investigated the ability of Pt1 and Pt2 to induce apoptotic cell death in SK-OV-3/DDP tumor cells by flow cytometry, and the results indicated that Pt2 induced apoptotic

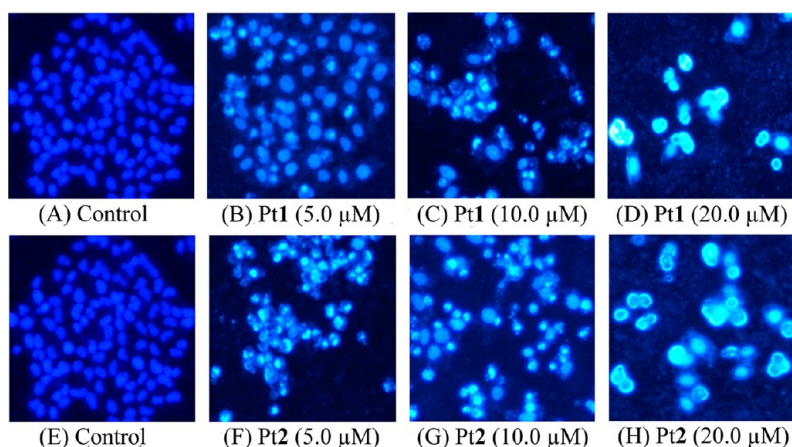


Figure 5. Morphological changes in the nuclei (typical of apoptosis) of cultured SK-OV-3/DDP cancer cells. SK-OV-3/DDP cancer cells treated with 5.0, 10.0, and 20.0 μM Pt1 and Pt2 for 12 h, respectively, and stained with Hoechst 33258. Selected fields illustrating occurrence of apoptosis were shown. Cells with condensed chromatin (brightly stained) were defined as apoptotic SK-OV-3/DDP cancer cells. Images were acquired using a Nikon Te2000 deconvolution microscope (magnification 200 \times).

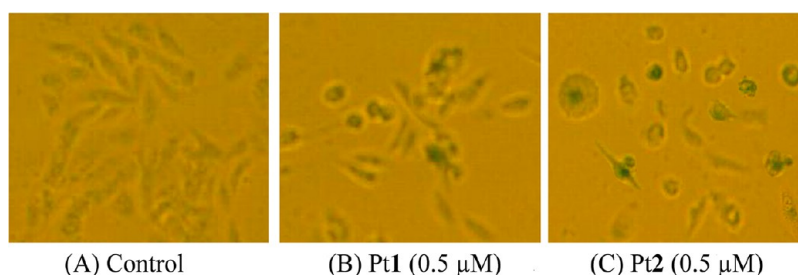


Figure 6. Expression of SA- β -Gal in SK-OV-3/DDP cells after continuous treatment with Pt1 and Pt2. SK-OV-3/DDP cells were treated with 0.5 μM Pt1, Pt2 or 0.1% DMSO (control) continuously for 7 days. Then the cells were fixed, stained with SA- β -Gal staining kit, and photographed. Images were acquired using a Nikon Te2000 deconvolution microscope (magnification 100 \times).

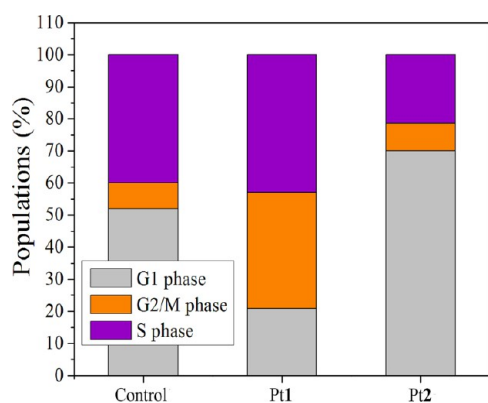


Figure 7. Effect of cell cycle of SK-OV-3/DDP treated with 5.0 μM of Pt1, Pt2 for 48 h compared with untreated cells. The percentages of cells in the different phases of cell cycle are reported inside the relative histogram.

cell death in a dose-dependent manner, as demonstrated by combined staining with annexin V-FITC (which detects phosphatidylserine residues translocated from the inner to the outer cell membrane in early apoptotic stages) and propidium iodide (PI, which stains necrotic cells) (Figure 8). In contrast, Pt1 failed to induce significant early stage apoptosis under the same conditions.

Detection of 53BP1, TRF1, and TRF2 by Immunofluorescence and Western Blotting. Telomeres are heterochromatic structures found at the ends of linear

eukaryotic chromosomes. Mammalian telomeres consist of several kilobases of tandem TTAGGG repeats bound by the related telomere-specific proteins, TRF1 and TRF2.²⁹ TRF1 negatively controls telomere length by cis-inhibiting telomerase activity. Overexpression of wild type TRF1 leads to telomere shortening, whereas inhibition of TRF1 with a dominant-negative mutant allele leads to telomere lengthening.³⁰ TRF2 is a key component of human telomere protein complex. TRF2 also binds to duplex telomeric repeats as a homodimer.³¹ Like TRF1, overexpression of intact TRF2 results in progressive telomere shortening too.³² Meanwhile, TRF2 deletion leads to telomere dysfunction and TIF formation. TIF is formed by the association of damaged telomeres with DNA damage response factors, such as 53BP1, ATM, γ -H2AX, Rif1, and the Mre11 complex.^{33a,b} Furthermore, 53BP1 binds to the tumor suppressor protein p53 and has a potential role in DNA damage responses.^{33c} Therefore, to clarify the effects of Pt1 and Pt2 on telomere dysfunction, we preferred to detect the expression of 53BP1, TRF1, and TRF2 in SK-OV-3/DDP cells by immunofluorescence and Western blotting (Figures 9–11). As shown in Figures 9 and 10, compared to the control group, the treatment of cells with Pt2 (4.5 μM) resulted in remarkable overexpression of 53BP1 (green in the merged images), TRF1 (fuchsia in the merged images), and TRF2 (fuchsia in the merged images), suggesting that Pt2 significantly induced DNA damage (overexpression of 53BP1) and telomeres damage (overexpression of TRF1 and TRF2) in SK-OV-3/DDP cells. Moreover, it was reported that TRF1 and TRF2 were two negative regulators of telomere length.^{33d} In the present study,

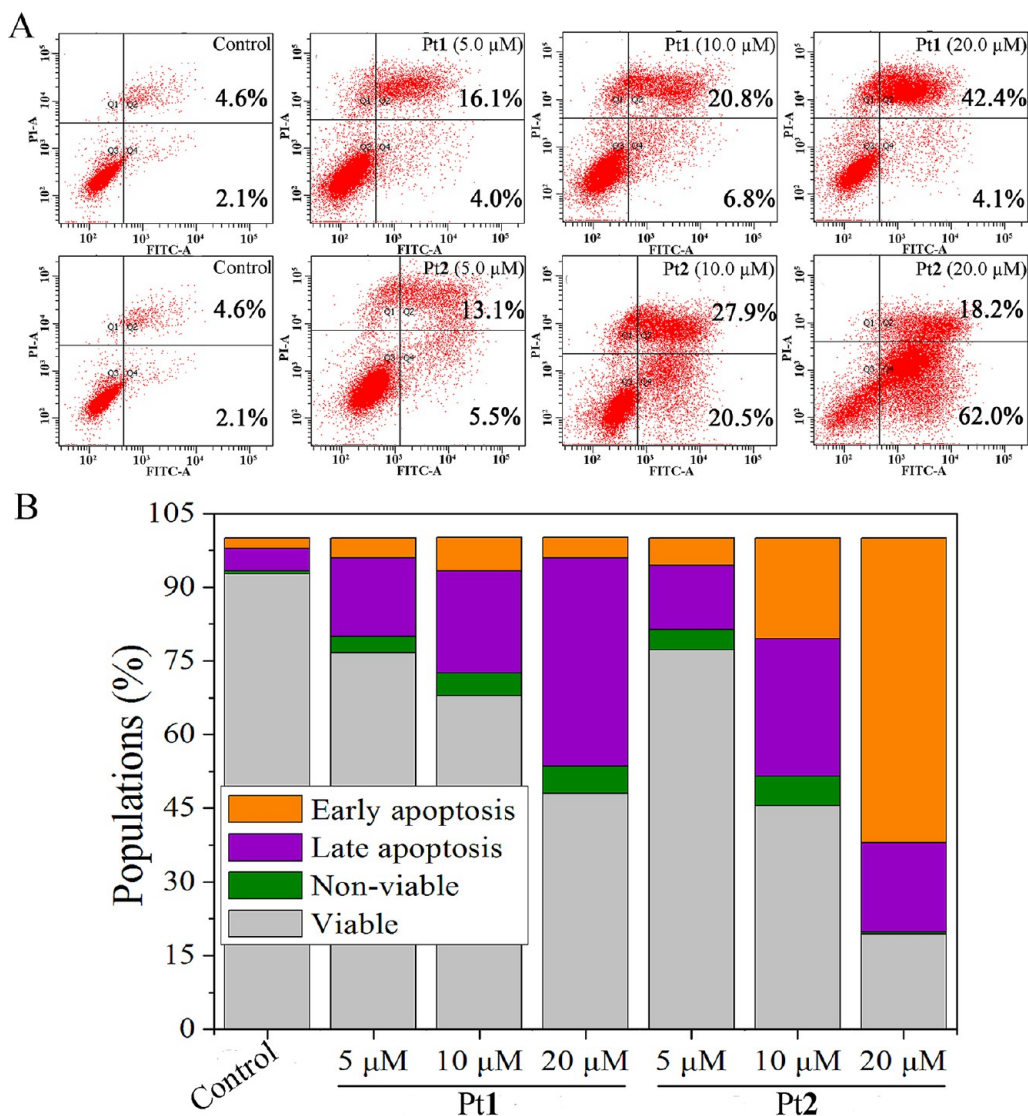


Figure 8. Effect of cell apoptosis of SK-OV-3/DDP treated with Pt1 and Pt2 for 12 h compared with the untreated cells. (A) The induction of apoptosis by Pt1 and Pt2 was examined by FACS analysis with PI and FITC-annexin V staining. (B) Populations for the apoptotic cells treated by Pt1 and Pt2.

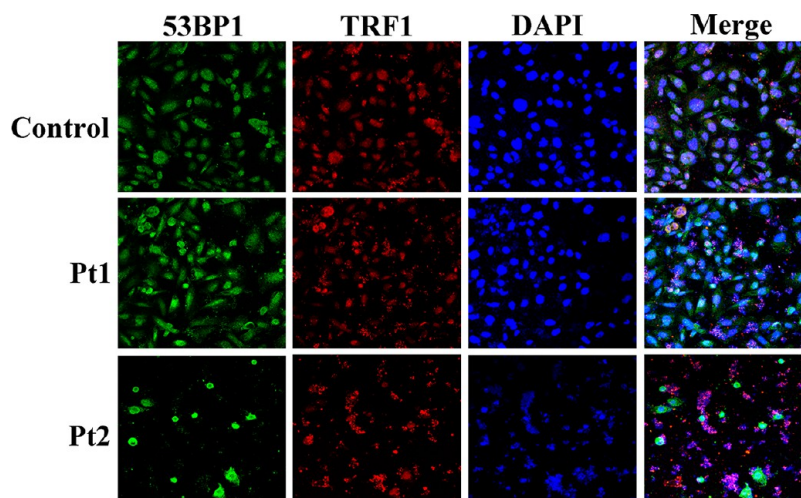


Figure 9. Binding of 53BP1 and TRF1 to uncapped telomeres. SK-OV-3/DDP cells were treated with 4.5 μM Pt1 and Pt2 for 12 h, respectively, and then were processed for 53BP1 (green) and TRF1 (red). The nuclei were stained (DAPI, blue) in the merged images. Images were acquired using a CarlZeiss LSM 710 microscope (magnification 400×).

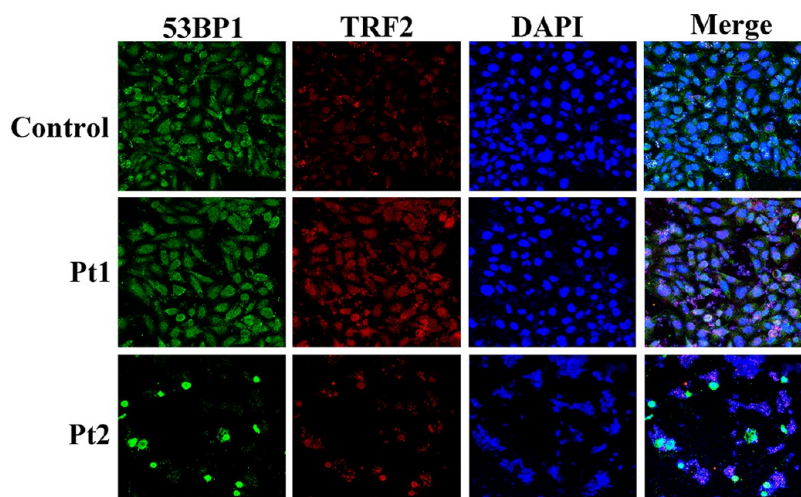


Figure 10. Binding of 53BP1 and TRF2 to uncapped telomeres. SK-OV-3/DDP cells were treated with $4.5 \mu\text{M}$ Pt1 and Pt2 for 12 h, respectively, and then were processed for 53BP1 (green) and TRF2 (red). The nuclei were stained (DAPI, blue) in the merged images. Images were acquired using a CarlZeiss LSM 710 microscope (magnification $400\times$).

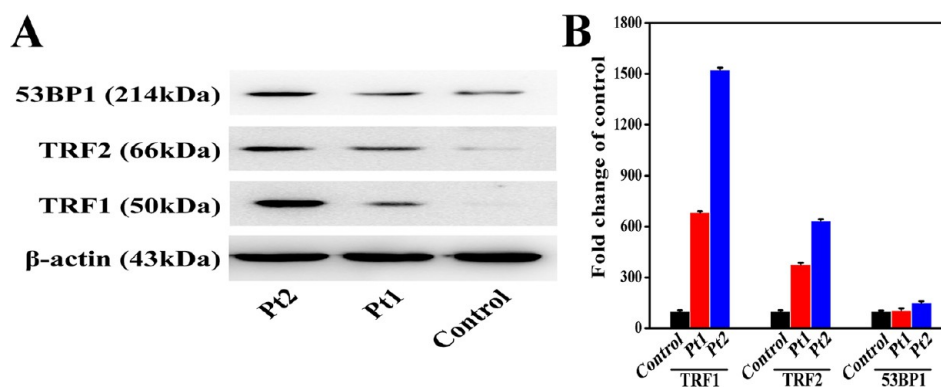


Figure 11. (A) Western blot to determine the translation of 53BP1, TRF1, and TRF2 in SK-OV-3/DDP cells treated with Pt1 ($4.5 \mu\text{M}$) and Pt2 ($4.5 \mu\text{M}$) for 12 h. (B) Densitometric analysis of 53BP1, TRF1, and TRF2 fragment normalized to β -actin band from part A. The relative expression of each band is (density of each band)/(density of actin band). Mean and SD values were from three independent measurements.

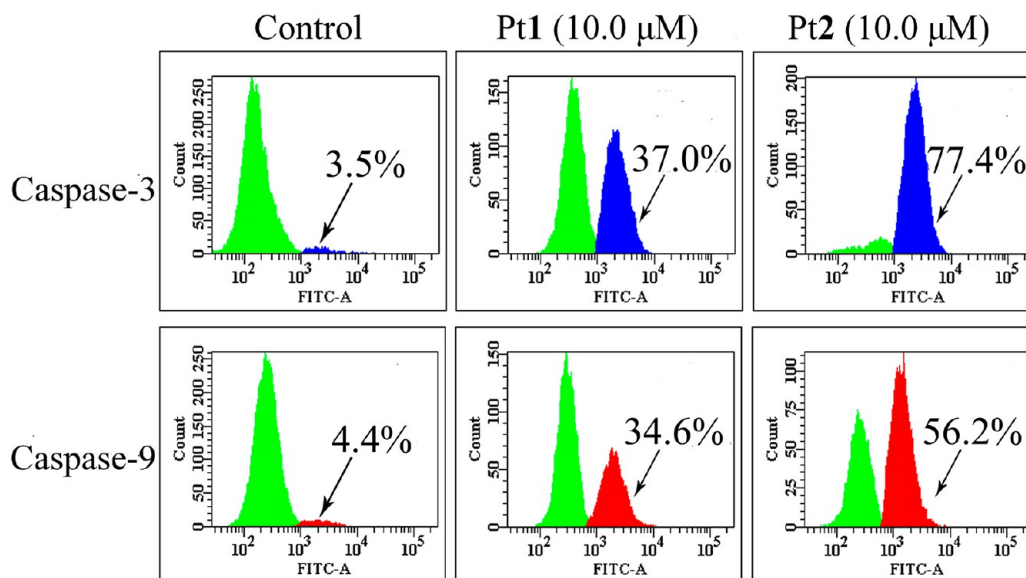


Figure 12. Expression level of caspase-3/9 proteins in SK-OV-3/DDP cells with $10.0 \mu\text{M}$ Pt1 or Pt2 for 8.0 h. Caspase-3/9 was assessed by the CasPGLOW fluorescein activate caspase-3/9 staining kits.

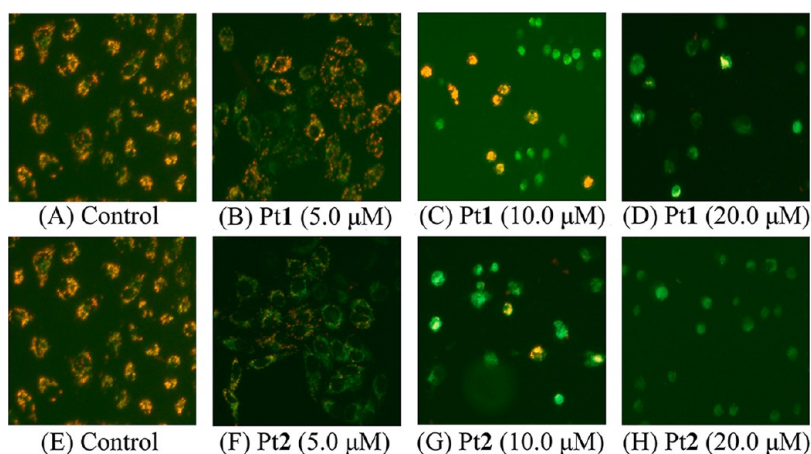


Figure 13. Representative photos of SK-OV-3/DDP cancer cells by JC-1 staining: polarized mitochondria are marked by punctuate orange-red fluorescence staining. On depolarization, the orange-red punctuate staining is replaced by diffuse green monomer fluorescence. Apoptotic cells, showing primarily green fluorescence, are easily differentiated from healthy cells, which show red and green fluorescence. Parts A and E represent the control without apoptosis. Parts B, C, D represent the 5.0, 10.0, 20.0 μM Pt1-treated samples with apoptotic SK-OV-3/DDP cancer cells, respectively. Parts F, G, H represent three concentrations of Pt2 with apoptotic SK-OV-3/DDP cancer cells, respectively. Images were acquired using a Nikon Te2000 deconvolution microscope (magnification 200 \times).

Table 2. FID Assay for L^a, L^b, Pt1, and Pt2 on DNA^a

	L ^a	Pt1	L ^b	Pt2
Pu27DC ₅₀ (ctDNA _{DC50} /Pu27DC ₅₀ [#])	6.37 (–)	1.35 (10.33)	15.13 (–)	0.55 (58.84)
c-kit-1DC ₅₀ (ctDNA _{DC50} /c-kit-1DC ₅₀)	>100 (–)	5.76 (2.42)	>100 (–)	2.42 (13.37)
c-kit-2DC ₅₀ (ctDNA _{DC50} /c-kit-2DC ₅₀)	>100 (–)	3.49 (4.00)	>100 (–)	3.46 (9.35)
HTG21DC ₅₀ (ctDNA _{DC50} /HTG21DC ₅₀)	40.58 (–)	2.50 (5.58)	16.65 (–)	1.31 (24.69)
Pu39DC ₅₀ (ctDNA _{DC50} /Pu39DC ₅₀)	>100 (–)	4.04 (3.45)	>100 (–)	1.52 (21.29)
mutPu39DC ₅₀ (ctDNA _{DC50} /mutPu39DC ₅₀)	60.98 (–)	4.23 (3.30)	>100 (–)	11.23 (2.88)
Pu22DC ₅₀ (ctDNA _{DC50} /Pu22DC ₅₀)	>100 (–)	6.02 (2.32)	>100 (–)	1.94 (16.68)
ds26DC ₅₀ (ctDNA _{DC50} /ds26DC ₅₀)	>100 (–)	7.43 (1.88)	>100 (–)	6.24 (5.19)
ctDNA _{DC50} (ctDNA _{DC50} /ctDNA _{DC50})	>100 (1.00)	13.95 (1.00)	>100 (1.00)	32.36 (1.00)

^a“–” indicates that no data can be calculated. # stands for G4-FID selectivity, defined as $\frac{\text{ctDNA}_{\text{DC}_{50}}}{\text{G}^4\text{DC}_{50}}$ ratio.^{35a} DC₅₀ obtained in μM .

it was found that the percentage of TRF1- and TRF2-induced telomeres damage by Pt2 was 72.33%. In contrast, less telomeres damage induction (48.26%) on SK-OV-3/DDP cells was observed when treated with Pt1 under the same conditions. These results suggested that the DNA damage response foci at telomeres induced by Pt2 were over other chromosomal regions. The selectivity of Pt2 for telomeric regions is better than that of Pt1.

Furthermore, the expression of 53BP1, TRF1, and TRF2 protein in the SK-OV-3/DDP cells treated with Pt1 and Pt2 was further identified using Western blotting. As shown in Figures 11, compared with the control group, Pt2 led to 151.04 \pm 8.07%, 1522.92 \pm 14.76%, and 632.584 \pm 10.25% increase of 53BP1, TRF1, and TRF2 protein expression level, respectively. The results indicate that Pt2 can induce telomere dysfunction and DNA damage. Comparatively, the Pt1 induced a weak increase of the expression of 53BP1, TRF1, and TRF2 protein on SK-OV-3/DDP cells under the same conditions (the accumulation of 53BP1, TRF1, and TRF2 of 106.02 \pm 12.37%, 682.55 \pm 9.91%, and 376.47 \pm 9.91%, respectively). The results agreed with DNA damage of immunofluorescence in the SK-OV-3/DDP cells.

Caspase-3/9 Activation Assay. The well characterized caspase family plays a crucial role in modulating programmed cell death, which is a genetically regulated and evolutionarily conserved process with numerous links to many human

diseases, most notably cancer. Caspase-3/9, the executioner caspase, is able to directly degrade multiple substrates including structural and regulatory proteins.³⁴ Thus, therapeutic strategies designed to stimulate apoptosis by activating caspase-3/9 may help in combating cancer caused by deficient apoptosis. Some small molecules have been developed to selectively activate caspase-3/9. We thus investigated whether the effector caspase-3/9 is activated when SK-OV-3/DDP cells are exposed to Pt1 and Pt2. As shown in Figure 12, cells treated with Pt1 and Pt2 exhibited a significant increase in caspase-3/9 activity, as indicated by the activation of caspase-3 in Pt1- and Pt2-treated cells (by 37.0% and 77.4%, respectively) and by the activation of caspase-9 in Pt1 and Pt2 groups (by 34.6% and 56.2%, respectively), compared with the control group. The results suggested that Pt1 and Pt2 are efficient activators of caspase-3/9, and Pt2 is more effective than Pt1. The activation of caspase-3/9 is an important pathway in Pt1- and Pt2-induced SK-OV-3/DDP apoptosis.

Assessment of Changes in Mitochondrial Membrane Potential. The loss of mitochondrial membrane potential is a characteristic of apoptosis. In nonapoptotic cells, JC-1 exists as a monomer in the cytosol (green) and accumulates as aggregates in the mitochondria (orange-red). In apoptotic and necrotic cells, JC-1 exists in monomeric form and stains the cytosol green. The control cells exhibited punctate orange-red staining (Figure 13A), indicating coupled mitochondria with a

normal $\Delta\psi$. As shown in Figure 13B, a few SK-OV-3/DDP cancer cells showed green fluorescence, which indicated that they were apoptotic cells with 5.0 μM Pt1 treatment. However, Figure 13C and Figure 13D show increased numbers of SK-OV-3/DDP cancer cells with green fluorescence, suggesting that Pt1 induced apoptosis in SK-OV-3/DDP cancer cells. Similar results were also observed with Pt2-treated SK-OV-3/DDP cancer cells. All Pt1/2-treated SK-OV-3/DDP cancer cells appeared green at 20 μM (Figure 13D and Figure 13H), but as shown in Figure 13F and Figure 13G, Pt2 induced more obvious apoptosis of SK-OV-3/DDP cancer cells compared with Pt1.

Selectivity for Binding of G-Quadruplex and Duplex DNA by L^a, L^b, Pt1, and Pt2 Determined by Spectroscopic Methods. The binding ability of L^a, L^b, Pt1, and Pt2 to G-quadruplex and duplex DNA was studied using FID assay, fluorescence titration analysis, circular dichroism (CD) spectral analysis, FRET assay, and ESI-MS (for detailed results, discussion, and experiments, see Supporting Information). As shown in Table 2, the FID assay results indicated that Pt1 and Pt2 exhibited better selectivity for HTG21 and Pu27 G-quadruplex DNAs than to other DNAs, which are the most efficient TO displacers (^{Pu27}DC₅₀ down to 1.35 and 0.55 μM with Pt1 and Pt2, ^{HTG21}DC₅₀ down to 2.50 and 1.31 μM with Pt1 and Pt2, respectively, also as shown in Table S4 and Figures S21 and S22). The selectivity of Pt1 and Pt2 for G4-DNA over duplex DNA is moderate, with ^{cDNA}DC₅₀/^{G4}DC₅₀ ratio (or Est. Sel.)^{35a} within the range of 1.88- and 10.33-fold and 2.88- and 58.84-fold, respectively. As expected, Pt2 with a 6-hydroxyl group in L^b has higher selectivity for quadruplex-DNA than Pt1. The data from fluorescence titration analysis and circular dichroism (CD) spectral analysis show that the binding of L^a, L^b, Pt1, and Pt2 with G-quadruplex DNA might increase the stability of the structure of G4-DNA and hence interfere with the DNA function. The results of fluorescence titration analysis and CD indicated that HTG21, Pu39, and mutPu39 DNAs preferentially folded into an intramolecular mixed G-quadruplex^{35b-d} in the solutions containing K⁺, while the Pu27 DNA preferred to form a parallel conformation^{35e} (as shown in Tables S5 and S6 and Figures S23–S34). As shown in Table 3, the FRET results demonstrated clearly that 2 μM Pt1

and Pt2 produced the ΔT_m values of 6.83 and 8.54 °C for F21T, 12.83 and 14.54 °C for FPu18T, respectively. Under 0.5 μM Pt1 and Pt2, the ΔT_m values for FMidG4T were 4.45 and 6.77 °C, respectively. However, under the same conditions, the ΔT_m values for duplex DNA (F32T + H20M) generated by Pt1 and Pt2 were 2.74 and 2.32 °C, respectively. Therefore, L^a, L^b, Pt1, and Pt2 exerted a weaker stabilizing effect of the duplex DNA (F32T + H20M) than F21T, FPu18T, and FMidG4T G-quadruplex DNA (Figure S35–S39). Moreover, Pt2 with a 6-hydroxyl group in L^b has higher selectivity for the quadruplex-DNA over duplex-DNA than Pt1. Taken together, Pt2 was favored to bind with the human telomeric G-quadruplex and G-quadruplex in the promoter region of c-myc and bcl-2, showing a relatively high thermodynamic stability, high binding constants, and a strong ability to induce conformational change in G-quadruplex. In addition, the ESI-MS results indicated that Pt1 and Pt2 covalently coordinated to guanine of G4-DNA (Figure S40).^{35fg}

Interactions with GSH. As one of the most widely distributed intracellular reductants, GSH also plays an important role in metal detoxification.³⁶ To date, a quantitative study has shown that GSH is a crucial contributor to protect against platinum cytotoxicity, and it may function in concert with or independently of glutathione or metallothionein.³⁷ At the same time, in some platinum-resistant cancer cells, glutathione and metallothionein levels are relatively high, which can neutralize the activated platinum effectively in the cytoplasm before DNA binding occurs. Therefore, we further explored the interaction of Pt1 and Pt2 with GSH. As shown in Figure S41 (Supporting Information), the absorbance of Pt2 at 463 nm exhibited a small decrease while the absorbance at about 245 nm increase upon the addition of GSH. Compared with Pt2, only obvious absorption changes at about 245 nm were observed in the UV spectra upon addition of GSH to the solution of Pt1. Interestingly, the result is closely correlated with the cytotoxicity of the two complexes. The GSH-reactive Pt1 and Pt2 are biologically active in tumor cells. Upon entering tumor cells, Pt1 and Pt2 do not react with GSH; therefore, their cytotoxicity in tumor cells is retained, which agrees well with the fact that Pt1 and Pt2 exhibited high activity against the cisplatin-resistant SK-OV-3/DDP cells.

Transcription and Translation of hTERT and c-myc Gene. Telomerase catalyzes the elongation of telomere, which involves complicated processes, such as the association and dissociation of catalytic enzyme. G-quadruplex ligands may affect the event mainly via two pathways, regulation of hTERT and c-myc, or stabilization of the telomeric G-rich end to block the association with the catalytic enzyme.³ Meanwhile, hTERT is the key catalytic domain of the telomerase enzyme, which is closely related to telomerase function and regulated by c-myc protein.³⁸ Because of the weak inhibitory activity of L^a and L^b in telomerase activity assay, only Pt1 and Pt2 were selected for quantitative RT-PCR and Western blot assay. Total RNA from SK-OV-3/DDP cells was extracted and reversely transcribed into cDNA to investigate the effect of the two Pt(II) complexes on c-myc and hTERT gene transcription. The cDNA was then used as a template in the specific amplification of c-myc and hTERT sequence by real-time PCR, with glyceraldehyde phosphate dehydrogenase (GAPDH) as internal control.

As shown in Figure 14A, generally, both Pt1 and Pt2 could increase the related protein products of hTERT with the increase of Pt1 and Pt2 concentrations. To further study the translation of hTERT gene, whole cell lysate of SK-OV-3/DDP

Table 3. ΔT_m Data (°C) of G-Quadruplex DNA Obtained by RT-PCR

compd	concn of compd	DNA (0.5 μM)	T_m (°C)	ΔT_m (°C)
L ^a	2.0 μM (0.5 μM)	F21T	53.65	4.45 (2.62)
	1.5 μM (0.5 μM)	FPu18T	70.72	11.95 (4.25)
	0.5 μM	FMidG4T	58.70	2.69
Pt1	2.0 μM (0.5 μM)	F32T + H20M	29.42	2.27 (0.67)
	2.0 μM (0.5 μM)	F21T	53.65	6.83 (2.68)
	1.5 μM (0.5 μM)	FPu18T	70.72	12.83 (4.31)
	0.5 μM	FMidG4T	58.70	4.45
L ^b	2.0 μM (0.5 μM)	F32T + H20M	29.42	2.74 (0.24)
	2.0 μM (0.5 μM)	F21T	53.65	4.48 (2.65)
	1.5 μM (0.5 μM)	FPu18T	70.72	12.30 (4.28)
	0.5 μM	FMidG4T	58.70	2.75
Pt2	2.0 μM (0.5 μM)	F32T + H20M	29.42	1.82 (0.76)
	2.0 μM (0.5 μM)	F21T	53.65	8.54 (3.42)
	1.5 μM (0.5 μM)	FPu18T	70.72	14.54 (5.15)
	0.5 μM	FMidG4T	58.70	6.77
	2.0 μM (0.5 μM)	F32T + H20M	29.42	2.32 (0.39)

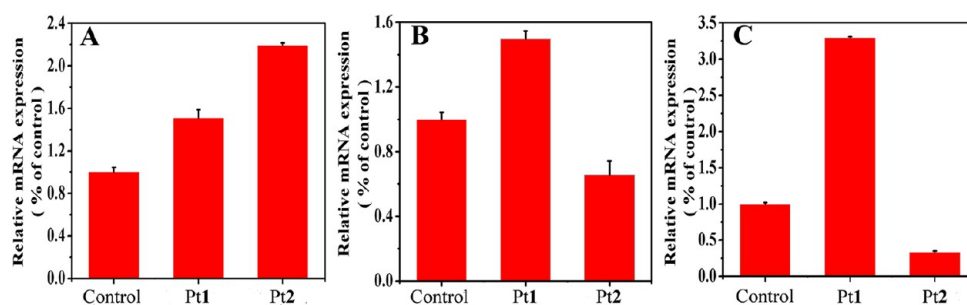


Figure 14. qRT-PCR to determine the expression of hTERT, c-myc, and bcl-2 in the SK-OV-3/DDP cell line treated with Pt1 and Pt2. 5×10^5 SK-OV-3/DDP cells were treated in a 25 cm² flask with medium (no drug), 5.0 μ M of Pt1 or Pt2 for 48 h, and the total RNA was extracted and subjected to reverse transcription, followed by PCR for hTERT (A), c-myc (B), or bcl-2 (C) and GAPDH (control).

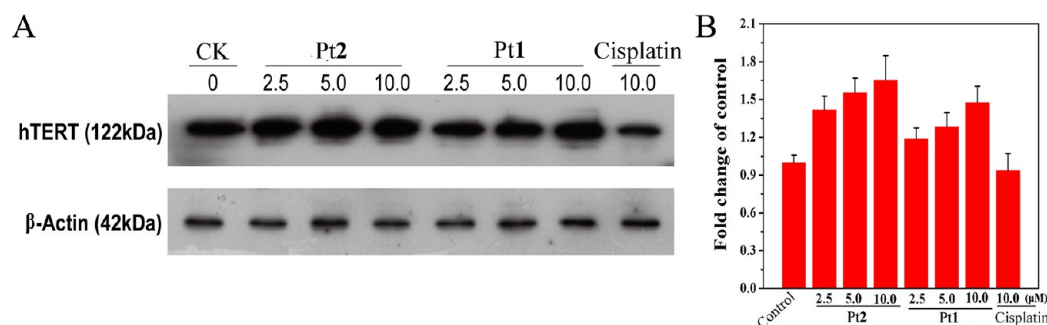


Figure 15. (A) Western blot to determine the translation of hTERT in SK-OV-3/DDP cell line treated with 2.5, 5.0, 10.0 μ M Pt1, Pt2 and cisplatin for 48 h. (B) Densitometric analysis of 122 kDa cleaved hTERT fragment normalized to 42 kDa β -actin band from part A. The relative expression of each band is (density of each band)/(density of actin band). Mean and SD values were from three independent measurements.

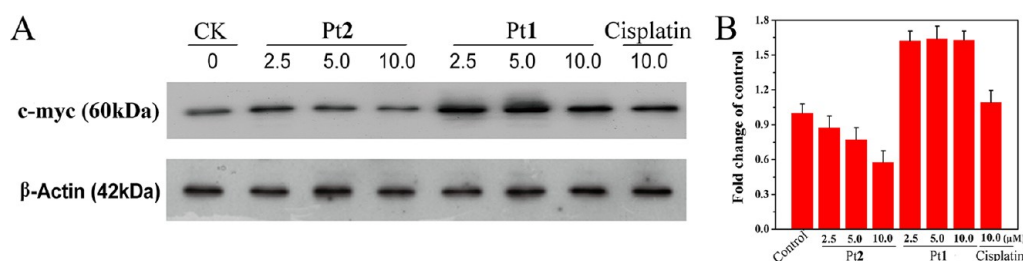


Figure 16. (A) Western blot to determine the translation of c-myc in SK-OV-3/DDP cells treated with 2.5, 5.0, 10.0 μ M Pt1, Pt2 and cisplatin for 48 h. (B) Densitometric analysis of 60 kDa cleaved c-myc fragment normalized to 42 kDa β -actin band from part A. The relative expression of each band is (density of each band)/(density of actin band). Mean and SD values were from three independent measurements.

cells was prepared, and hTERT protein was detected in Western blot analysis, with β -actin as loading reference. Figure 15 shows that both Pt1 and Pt2 were able to up-regulate the transcription and translation of oncogene hTERT in concentration-dependent mode; furthermore, Pt2 was more effective than Pt1. These results were further confirmed by RT-PCR and Western blot methods.

The inhibitory activity of Pt1 and Pt2 on the expression of c-myc gene was also studied using RT-PCR and Western blot assay. As shown in Figure 14B, Pt1 increased the protein products of c-myc compared with the control, whereas Pt2 down-regulated the transcription and translation of oncogene c-myc. Such observations were further confirmed by the Western blot results of the translation of c-myc in SK-OV-3/DDP cells treated with Pt1 and Pt2, respectively (Figure 16). All these results confirmed that binding of Pt1 to c-myc promoter region increased the promoter stability and up-regulated c-myc transcription, which further up-regulated the expression of hTERT, as detected by real-time RT-PCR. The same results were also observed by other groups;³⁹ e.g., our results are also

consistent with the previously reported association between myc overexpression and the induction of telomerase activity.³⁹ However, Pt2 could down-regulate the transcription of c-myc, which still further up-regulated the expression of hTERT in SK-OV-3/DDP cells. The mechanisms may be that after c-myc binds to E-box, it directly activates the expression of hTERT gene, and such activation is not correlated with cell proliferation and independent of de novo synthesis of proteins. Thus, although Pt2 inhibited c-myc expression, the gene hTERT was still overexpressed in cells.⁴⁰

Transcription and Translation of bcl-2 Gene. RT-PCR was carried out to investigate the effect of Pt1 and Pt2 on bcl-2 gene transcription in SK-OV-3/DDP cells. As shown in Figure 14C, Pt2 down-regulated the transcription of bcl-2; on the contrary, Pt1 increased the RNA level of bcl-2. While 10 μ M Pt2 led to a 65% decrease of bcl-2 mRNA level, Pt1 generated an opposite effect, suggesting that Pt1 and Pt2 exerted differential effects on bcl-2 gene transcription. These observations were further confirmed by Western blot analysis. As shown in Figure 17, Pt2 dose-dependently decreased the

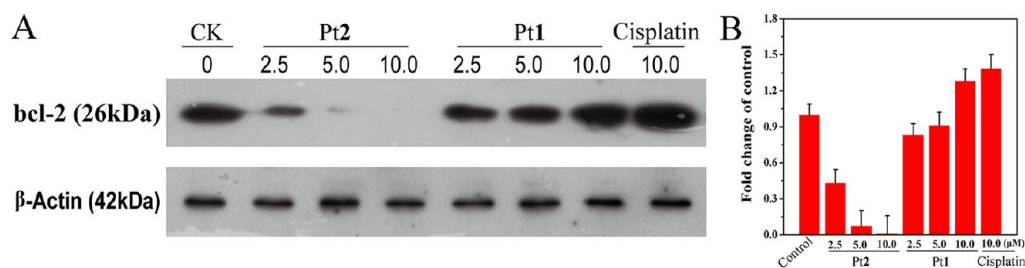


Figure 17. (A) Western blot to determine the translation of Bcl-2 in SK-OV-3/DDP cell lines treated with 2.5, 5.0, 10.0 μ M Pt1, Pt2 and cisplatin for 48 h. (B) Densitometric analysis of 26 kDa cleaved bcl-2 fragment normalized to 42 kDa β -actin band from part A. The relative expression of each band is (density of each band)/(density of actin band). Mean and SD values were from three independent measurements.

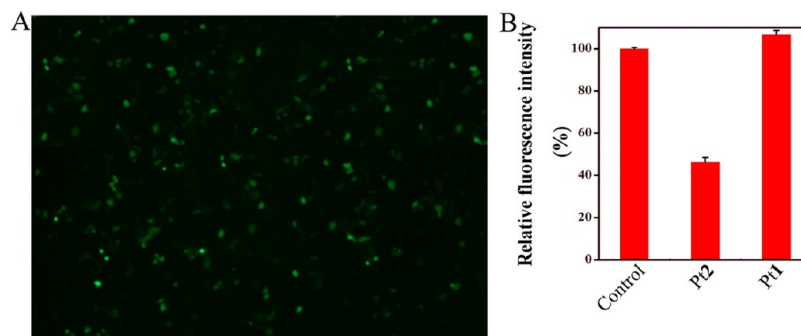


Figure 18. Transfections of EGFP (A) and c-myc (B) plasmid vector in SK-OV-3/DDP cells.

protein products of bcl-2, whereas Pt1 up-regulated the translation of bcl-2. These results verified that Pt2 could inhibit the activity of bcl-2 gene via its special interaction with the promoter region of Pu39,¹¹ but Pt1 did not undergo such pathway.

Transfection. In order to verify whether Pt1 and Pt2 can directly regulate c-myc promoter (Pu27) and the expression of hTRET in SK-OV-3/DDP cells, consequently inhibiting the telomerase function, we constructed EGFP and c-myc gene vectors according to the methods reported by Chalfie⁴¹ and He.⁴² After successful transfection of SK-OV-3/DDP cells, an amount of 5.0 μ M Pt1 and Pt2 was added to these cells, respectively, and incubated for 24 h. Subsequent fluorescent microscopy study showed that (Figure 18A) after EGFP plasmid transfection, SK-OV-3/DDP cells displayed green fluorescence, indicating a successful transfection. As shown in Figure 18B, in comparison with the control, Pt1 up-regulated the hTRET expression in SK-OV-3/DDP cells, resulting in inhibition of the activity of telomerase via activation of c-myc promoter, whereas Pt2 achieved these effects by down-regulating the activity of c-myc promoter. It is interesting that such different effects may correlate with the 6-hydroxy group at the 6-position of L^b in Pt2, which is in agreement with the results mentioned above.

Telomerase Inhibition (TRAP Assay). Many studies have shown that stabilization of G-quadruplexes or ligand-induced quadruplex formation by the telomeric G-rich strand can inhibit the activity of telomerase.^{8,18a,43} Telomerase is overexpressed in 85–90% of the human tumor cells but has undetectable activity in most of the normal somatic cells.⁴⁴ Therefore, we conducted TRAP assay to further characterize telomerase activity. Solutions of L^a, L^b, Pt1, and Pt2, respectively, were added to a telomerase reacting mixture containing extract from Hep-G2 cells,⁴⁵ which express high levels of telomerase. The inhibition ratios of L^a, L^b, Pt1, and Pt2 were summarized in Figure 19 and Table S7 (Supporting Information). As indicated in Table S7,

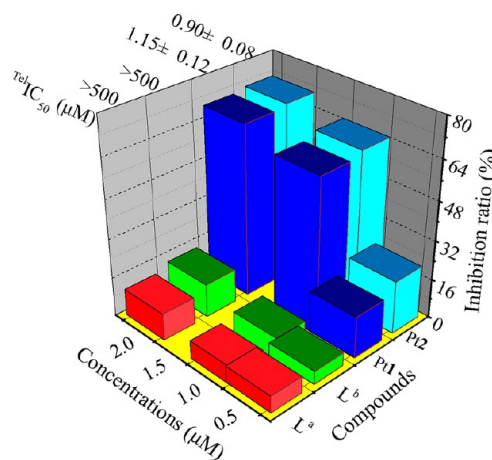


Figure 19. Inhibitory rates (%) and ^{Tel}IC₅₀ of L^a, L^b, Pt1, and Pt2 on telomerase.

the telomerase inhibition properties of Pt1 and Pt2 were significantly improved upon oxoisoaporphine alkaloids ligating Pt(II). It is interesting that the inhibitory potential on telomerase was enhanced with a hydroxy group at the 6-position of L^b in Pt2.

In order to further determine the ability of L^a, L^b, Pt1, and Pt2 to inhibit the telomerase in SK-OV-3/DDP tumor cells, we treated SK-OV-3/DDP cells with 5.0 μ M L^a, L^b, Pt1, and Pt2, respectively, for 48 h. The telomerase activity was assayed using a PCR-TRAP ELISA kit (Roche, USA) according to the manufacturer's guide. As shown in Figure 20, the cellular inhibitory effect of Pt1 and Pt2 on telomerase was obviously higher than that of L^a and L^b; moreover, the telomerase inhibitory property of Pt2 was significantly better than that of Pt1, which agrees well with the results of FRET and CD assays. Together the above studies indicated that Pt1 could exert

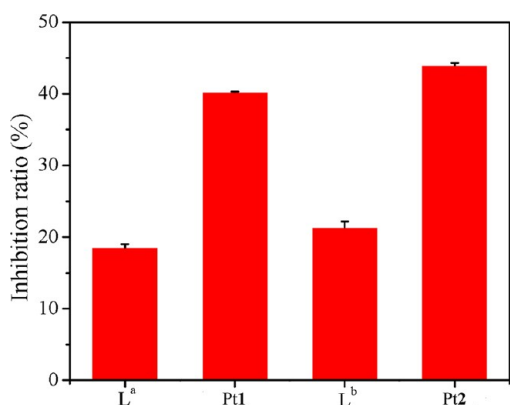


Figure 20. Inhibitory rates (%) of L^a, L^b, Pt1, and Pt2 on telomerase in SK-OV-3/DDP tumor cells.

effects by up-regulating the transcription and translation of c-myc, hTERT, and bcl-2 genes, while Pt2 might play its role via other pathways in SK-OV-3/DDP tumor cells.

Protein Binding Studies. Anticancer activity may be strongly affected by drug–protein interactions in the bloodstream. Serum albumin, the most abundant and important protein in the plasma, is the major transport protein. Albumin is capable of binding many endogenous and exogenous drugs reversibly. In addition, it may aid in the selective delivery of drugs to the tumor region and facilitate drug access into the cell.⁴⁶ The tryptophan emission quenching experiments were carried out to investigate the interaction of Pt1 and Pt2 with proteins by using bovine serum albumin (BSA) as model protein. Generally, the fluorescence of BSA is derived from two

intrinsic characteristic amino acids of the protein, i.e., tryptophan and tyrosine. Changes in the emission spectra of tryptophan are common in response to protein conformational transitions, subunit associations, substrate binding, or denaturation. Therefore, the intrinsic fluorescence of BSA can provide considerable information on their structure and dynamics and is often utilized in the study of protein folding and association reactions. The quenching of emission intensity of BSA was observed in the presence of the complex because of the changes in tryptophan environment resulting from possible changes in BSA protein secondary structure.⁴⁷

The interactions of BSA with Pt1 and Pt2 were studied by fluorescence spectroscopy at 296, 303, and 310 K. The BSA solution (0.5 μ M) was titrated with various concentrations of Pt1 and Pt2 (0–8 μ M), respectively. The effects of Pt1 and Pt2 on the fluorescent emission spectra of BSA are shown in Figures S42 and S43 and Table S9 (Supporting Information). The addition of Pt1 and Pt2 to the solution of BSA resulted in a significant decrease of the fluorescent intensity of BSA at 345 nm, suggesting a definite interaction of Pt1 and Pt2 with BSA protein.⁴⁸

In the case of Pt1, the Stern–Volmer constants were calculated from the slope of the plot F_0/F versus [Pt1] (Figures S42 and S43), and the values were found to be $0.80 \times 10^5 \text{ M}^{-1}$ (296 K), $0.87 \times 10^5 \text{ M}^{-1}$ (303 K), and $1.33 \times 10^5 \text{ M}^{-1}$ (310 K), respectively (Table S9). However, the K_{sv} of Pt2 was not suitable to calculate by Stern–Volmer equation because the correlation between F_0/F and [Pt2] was nonlinear. These results suggested that Pt2 exhibited higher binding affinity than Pt1, and the quenching of both Pt1 and Pt2 was dynamic.

Growth Inhibition of HCT-8 and NCI-H460 Xenograft in Vivo. To test the efficacy of Pt1 and Pt2 to inhibit tumor

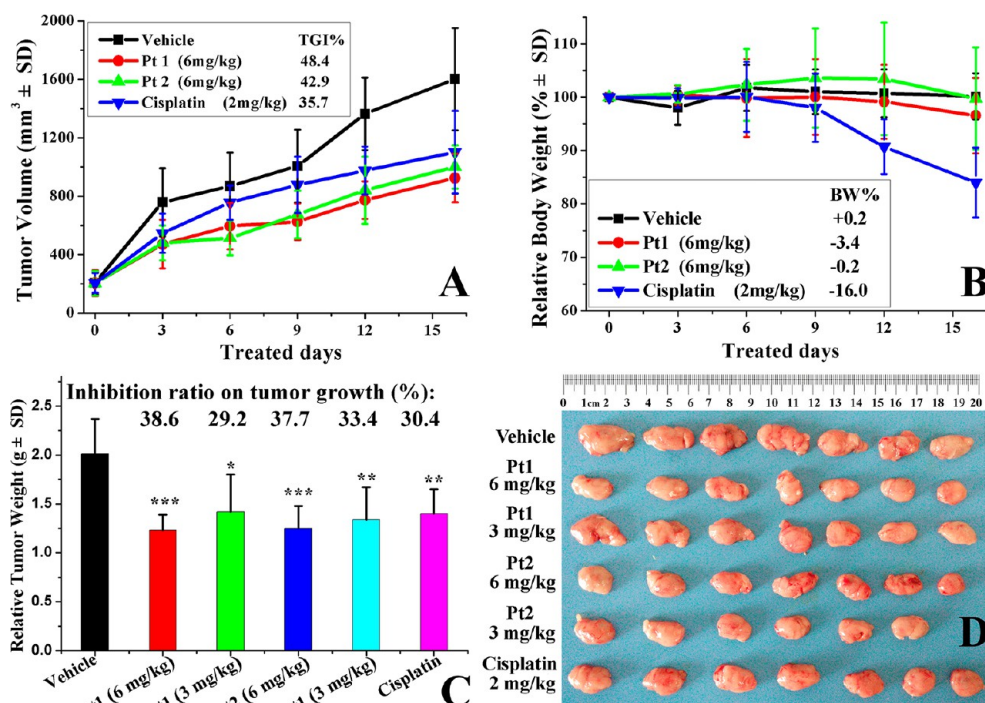


Figure 21. In vivo anticancer activity of Pt1 and Pt2 in mice bearing HCT-8 xenograft. (A) Effect of Pt1, Pt2 ((6 mg/kg)/2 days), cisplatin ((2 mg/kg)/2 days), or vehicle (5% DMSO in saline, v/v) on growth of tumor xenograft. Tumor growth is tracked by the mean tumor volume (mm³) \pm SD ($n = 6-7$) and calculated as % tumor growth inhibition (%TGI). (B) Body weight change (presented as % change from initial weight). (C) Tumor weight was recorded after the mice were killed: (***) $P < 0.001$, (**) $P < 0.01$, (*) $P < 0.05$. (D) Photographs of tumor from treatment groups and vehicle group.

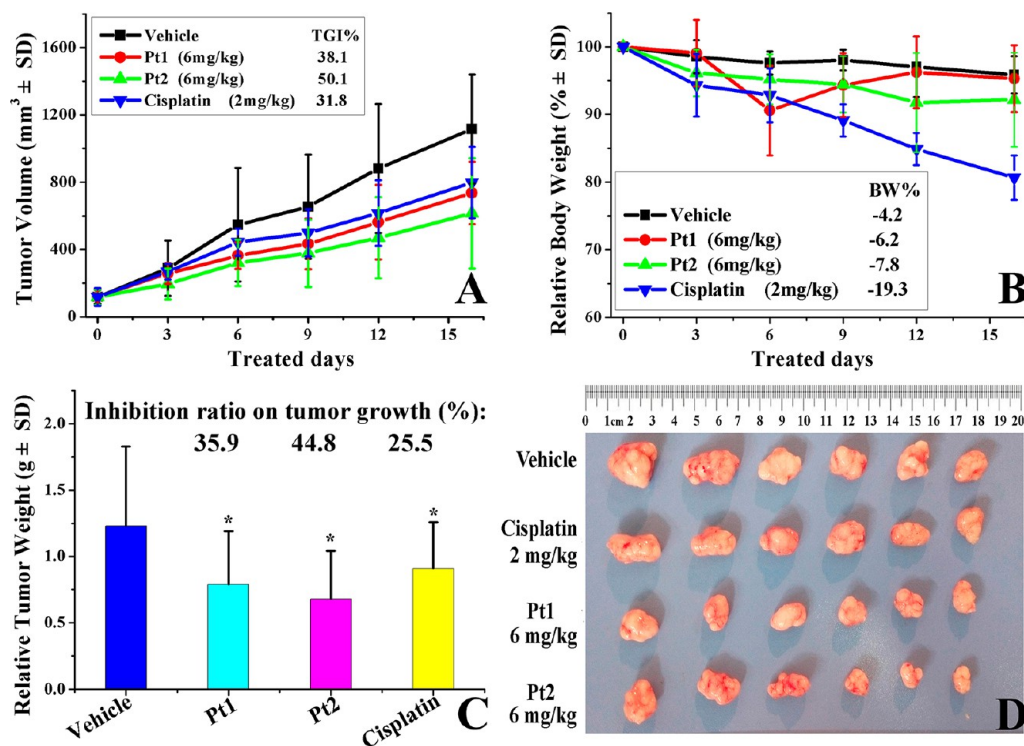


Figure 22. In vivo anticancer activity of Pt1 and Pt2 in mice bearing NCI-H460 xenograft. (A) Effect of Pt1, Pt2 ((6 mg/kg)/2 days), cisplatin ((2 mg/kg)/2 days), or vehicle (5% DMSO in saline, v/v) on growth of tumor xenograft. Xenograft was established sc in athymic mice and allowed to reach a volume of 100–300 mm³ before treatment. Data represent tumor volumes as mean ± SD ($n = 6$) and calculated as % tumor growth inhibition (%TGI). (B) Body weight change (presented as % change from initial weight). (C) Tumor weight was recorded after the mice were killed: (*) $P < 0.05$. (D) Photographs of tumor from treatment groups and vehicle group.

growth in vivo, the HCT-8 and NCI-H460 tumor xenograft nude mice were used. In the two models, mice with tumors at the volume of 100–300 mm³ were randomized into vehicle control and treatment groups ($n = 6-7$ /group) and treated via ip injection with Pt1, Pt2, and cisplatin, respectively, every other day. As shown in Figure 21A and Figure 21B, treatment groups were injected with Pt1 and Pt2 at two doses (6 or 3 mg/kg)/2 days for 16 days in the HCT-8 tumor model and at one dose (6 mg/kg)/2 days in NCI-H460 model; cisplatin was injected at doses of 2 (mg/kg)/2 days, and control mice received the vehicle (5% DMSO in saline, v/v).

In the human colorectal tumor HCT-8 xenograft model, as shown in Figure 21 and Tables S10–S12 (Supporting Information), the treatment with Pt1 and Pt2 at 6 mg/kg resulted in a statistically significant reduction in tumor volume with tumor growth inhibition (TGI) of 48.4% and 42.9% respectively ($P < 0.001$ and $P < 0.01$, respectively, vs vehicle control group), which was greater than that of cisplatin (TGI, 35.7%). Similar results were observed in the tumor weight change (Figure 21C); i.e., at a dose of 6 mg/kg, Pt1 (inhibition rate, IR, 38.5%) and Pt2 (IR, 37.7%) displayed better antitumor activity than cisplatin (IR, 30.4%). In addition, the data showed that treatment with Pt1 presented a dose-dependent inhibition of tumor growth.

In the human lung cancer NCI-H460 xenograft model, as shown in Figure 22 and Tables S13–S15 (Supporting Information), after 16 days of treatment, Pt2 at a dose of 6 mg/kg caused a substantial reduction in both tumor volume and weight with a TGI of 50.1% and IR of 44.8% ($P < 0.05$). By contrast, Pt1 displayed a lower activity on NCI-H460 tumor growth in vivo (TGI, 38.1%; IR, 35.9%). However, both

complexes exhibited better antitumor activity than cisplatin (TGI, 31.8%; IR, 25.5%).

Throughout the treatment period, there was no significant difference in body weight change among the control group and Pt1- and Pt2-treated groups (Figure 21B), and the animals appeared healthy, with no visible signs of pain, distress, or discomfort. No signs of peritonitis or damage to organs were observed (Figure S44 in Supporting Information). Although cisplatin treatment also caused tumor growth inhibition, its toxicity was apparent, as evidenced by loss of body weight compared to vehicle control (Figure 22B).

The preliminary results indicated that Pt1 and Pt2 exhibited high safety in vivo and were even more effective in inhibiting tumor growth in the HCT-8 and NCI-H460 xenograft mouse models than cisplatin.

Structure–Activity Relationships. On the basis of the results mentioned-above on the biological activity and anticancer mechanism studies, some SAR trends between the L^a, L^b, Pt1, Pt2 and the differences in biological activity can be established. First, in general, the combination of platinum with corresponding oxoisoaporphine alkaloids L^a and L^b appears to produce an increase biological activity with respect to free ligands L^a and L^b. Second, excluding some exceptions, the homologous series of complexes Pt1, Pt2, differing only in the ligands, also show some structure–activity relationships. For example, against NCI-H460 and SK-OV-3/DDP, the presence of a 6-hydroxyl group in ligand (Pt2) seems to generate an increase in cytotoxicity with respect to the ligand lacking such hydroxyl group (Pt1). From the in vivo anticancer activity of Pt1 and Pt2 in mice bearing NCI-H460 xenograft, such SARs trend also was observed. Furthermore, the anticancer action

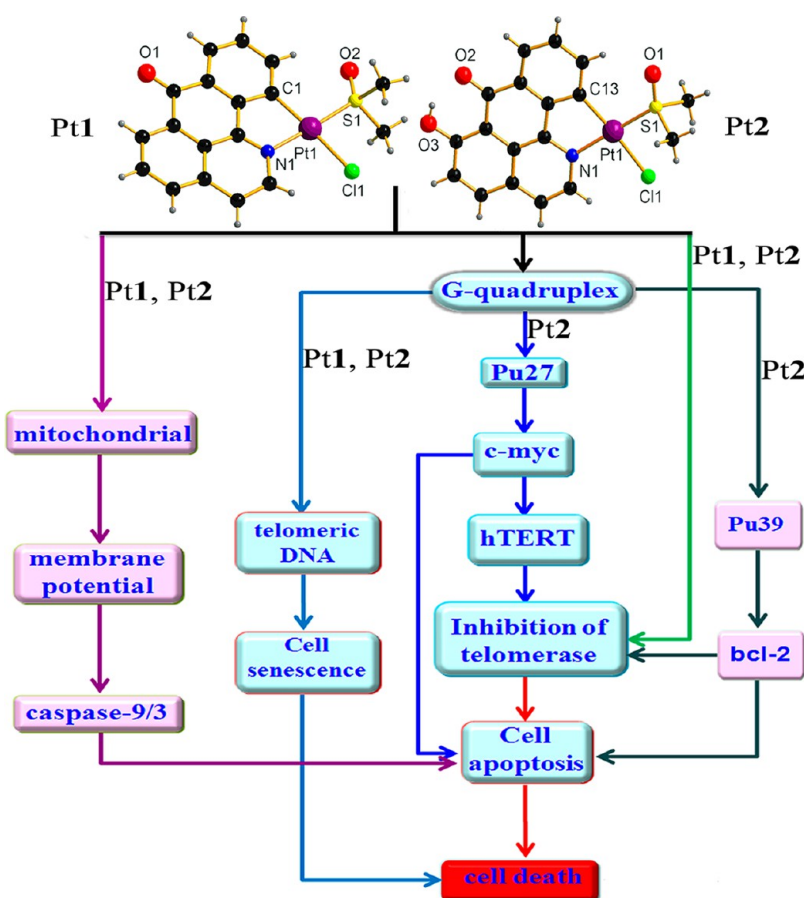


Figure 23. Proposed antitumor mechanisms for Pt1 and Pt2.

Table 4. Sequences of Oligomers (Primers) Used in This Work

oligomer	sequence
c-kit-1	5'-CGGGCGGGCACGAGGGAGGGT-3'
c-kit-2	5'-CGGGCGGGCGCTAGGGAGGGT-3'
HTG21	5'-GGGTTAGGGTTAGGGTTAGGG-3'
Pu22	5'-TGAGGGTGGGTAGGGTGGGTAA-3'
FMidG4T	5'-FAM-CGGGCGGGGAGGAAGGGGGCGGGAGC-TAMRA-3'
FPu18T	5'-FAM-AGGGTGGGGAGGGTGGGG-TAMRA-3'
F21T	5'-FAM-GGGCTAGGGCTAGGGCTAGGG-TAMRA-3'
ds26	5'-CAATCGGATCGAATTCGATCCGATTG-3'
Pu27	5'-TGGGGAGGGTGGGGAGGGTGGGGAAGG-3'
Pu39	5'-AGGGCGGGCGGGAGGAAGGGGGCGGGAGCGGGGCTG-3'
mutPu39	5'-AGGGGCAAACGCAAAGGAAAAAACGGGAGCGGGGCTG-3'
c-myc	Ts: 5'-TGGTGCTCCATGAGGAGACA-3' Cx: 5'-GTGGCACCTCTGAGGACCT-3'
GAPDH	Ts: 5'-GCCTCTTGCACGACCAACTG-3' Cx: 5'-CGGAAGGCCATGCCT GTCAG-3'
hTERT	Ts: 5'-TGGTCTCCACGAGCCTCCGAGCG-3' Cx: 5'-CATCCACATAGAGCCACCACGT-3'
F32T	5'-FAM-CCGCATCTCTACATTCAAGAACTGGCATGCCG-TAMRA-3'
H20M	5'-GCCAGTTCTTGAATGTAGAG-3'

mechanism studies also confirmed that such SARs might originate from different biological behavior of Pt1 and Pt2. It could be demonstrated that Pt2 with 6-hydroxy group in L^b exhibited stronger induction of cell senescence and apoptosis than Pt1 without 6-hydroxy group in L^a; Pt2 displayed stronger telomerase inhibition ability and better selectivity for G4-DNA

and telomeric region and led to more severe telomeres damage in SK-OV-3/DDP cells than Pt1.

CONCLUSION

To develop effective G-quadruplex DNA binders exerting inhibitory effect on telomerase activity, two oxoisoapopine-organoplatinum(II) complexes (Pt1 and Pt2) were prepared

and evaluated for antitumor activity in vitro and in vivo. The binding experimental results from various biological assays, including FID assay, FRET assay, fluorescence titration, and CD, revealed that Pt2 had relatively different but stronger binding affinity to G-quadruplex DNA in telomere and promoters of c-myc and bcl-2 than Pt1. Further cellular assays, including uptake assay, flow cytometry, RT-PCR, Western blotting, immunofluorescence, transfection, and TRAP assay, gave evidence that Pt1 and Pt2 exerted its antitumor effect on tumor cells. As shown in Figure 23, we propose the action mechanisms that the effect of Pt1 and Pt2 on tumor cells may involve the major pathways. Both complexes could activate caspase-3/9 to initiate cell apoptosis, and the effect of Pt2 appeared stronger. Pt2 arrested cell growth at G1 phase in contrast to Pt1 (at G2/M phase). Pt2 exerted its antitumor mechanism mainly via its inhibition of telomerase activity and interaction with telomeric, c-myc, and bcl-2 G-quadruplexes, and inducing senescence as well as apoptosis finally caused SK-OV-3/DDP tumor cells' death. Compared with Pt2, Pt1 also can induce senescence and apoptosis of SK-OV-3/DDP cells, for which the activity was weaker than that of Pt2, but its process was mainly mediated by apoptotic pathway owing to interaction with telomeric G-quadruplex, and inhibition telomerase activity. The different biological activities of Pt1 and Pt2 may be correlated with the structural feature of oxoisoaporphine ligand in Pt2, for L^b contains a 6-hydroxyl group, which is absent in the L^a of Pt1. Remarkably, our findings illustrated that Pt1 and Pt2 exhibited high safety in vivo and even more effective inhibitory effect on tumor growth in the HCT-8 and NCI-H460 xenograft mouse model than cisplatin. Taken together, the two organoplatinum(II) complexes Pt1 and Pt2 exhibited antitumor effects on SK-OV-3/DDP cells in vitro via both cell senescence- and cell apoptosis-mediated mechanisms. Therefore, Pt1 and Pt2 may have the potential to be further developed into safe and effective anticancer agents.

■ EXPERIMENTAL METHODS

Materials. All chemical reagents were commercially available and used without further purification, unless noted specifically. The purity of all target compounds used in the biophysical and biological studies was $\geq 95\%$. All compounds were routinely checked by HPLC. Thiazole orange (TO), Tris, RNase A, and propidium iodide (PI) were purchased from Sigma. 53BP1, TRF1, TRF2, bcl-2, hTERT, and c-myc were purchased from Abcam. DNA oligomers (highly polymerized stored at 4 °C; long-term storage at -20 °C) are listed in Table 4 and were obtained from Shanghai Sangon Biological Engineering Technology & Services (Shanghai, China). The DNA concentration per pair was determined based on the absorbance value at $\lambda = 260$ nm ($\epsilon_{260} = 3.81 \times 10^5$ M (strand)⁻¹ cm⁻¹ for DNA oligomers by using UV/vis absorption spectroscopy.⁴⁹ Unless otherwise stated, spectroscopic titration experiments were carried out in 10 mM Tris-HCl (pH 7.35) containing 100 mM KCl. Telomerase PCR ELISA kits were purchased from Roche (USA). The total RNA isolation kit and the two-step RT-PCR kit were purchased from TIANGEN. All tumor cell lines were obtained from the Shanghai Institute for Biological Science (China).

Stock solutions of all the compounds (2 mM) were made in DMSO. Further dilutions to working concentrations were made with corresponding buffer. The formation of all intramolecular G-quadruplexes was analyzed as follows: the oligonucleotide samples, dissolved in Tris-KCl-HCl buffer, were heated to 95 °C for 10 min, gently cooled to room temperature, and then incubated at 4 °C overnight. The human telomeric was extemporaneously prepared in

Tris-HCl buffer. All the spectroscopic experiments were performed at room temperature.

Instrumentation. Infrared spectra were obtained on a PerkinElmer FT-IR spectrometer. Elemental analyses (C, H, N) were carried out on a PerkinElmer series II CHNS/O 2400 elemental analyzer. NMR spectra were recorded on a Bruker AV-500 NMR spectrometer. Fluorescence measurements were performed on a Shimadzu RF-5301/PC spectrofluorophotometer. ESI-MS spectra were performed on Thermofisher Scientific Exactive LC-MS spectrometer (Thermal Electronic, USA). The circular dichroic spectra of DNA were obtained on a JASCO J-810 automatic recording spectropolarimeter operating at 25 °C. The region between 200 and 400 nm was scanned for each sample. MTT assay and fluorescent intercalator displacement (FID) assay were performed on M1000 microplate reader (Tecan Trading Co. Ltd., Shanghai, China). Cell cycle analysis results were recorded on FACS Aria II flow cytometer (BD Biosciences, San Jose, CA, USA). FRET assay was performed on 7500fast RealTime PCR (ABI Co. Ltd., USA).

Synthesis of 1-Azabenzanthrone (L^a) and Pt1. L^a was synthesized by using modified method reported by Tang et al.²⁴ The extract was condensed under reduced pressure, and the resultant precipitate was washed, dried, and sublimed at 130–140 °C at a pressure of 1 mmHg to give the product L^a as a light yellow solid. ¹H NMR (500 MHz, DMSO-*d*₆) δ 8.78 (dd, *J* = 5.6, 3.3 Hz, 2H), 8.52 (dd, *J* = 7.2, 1.1 Hz, 1H), 8.41 (dd, *J* = 8.2, 1.0 Hz, 1H), 8.25 (dd, *J* = 7.9, 1.2 Hz, 1H), 8.06–8.03 (m, 1H), 8.02–8.01 (m, 1H), 7.89 (td, *J* = 7.6, 1.4 Hz, 1H), 7.74–7.71 (m, 1H). ¹³C NMR (126 MHz, DMSO-*d*₆) δ 182.71, 147.96, 144.49, 136.59, 135.28, 134.76, 134.62, 132.20, 131.50, 131.10, 130.19, 128.54, 127.47, 125.37, 122.39, 121.92. ESI-MS *m/z*: 278.2 [M + CH₃CH₂OH + H]⁺. IR (KBr): 3434, 3056, 3005, 1983, 1667, 1613, 1596, 1580, 1438, 1393, 1292, 1218, 1205, 949, 851, 795, 754, 702, 650, 584 cm⁻¹. Elemental analysis calcd (%) for C₁₆H₉NO: C 83.10, H 3.92, N 6.06. Found: C 83.21, H 3.90, N 5.93.

The complex [PtL^a(DMSO)Cl] (Pt1) was prepared by treating L^a (0.0231 g, 0.1 mmol) with Pt(DMSO)₂Cl₂ (0.0422 g, 0.1 mmol) in ethanol/water (10:1) under solvothermal conditions. L^a deprotonation took place upon the addition of Pt(II) ion to the ligand solution to form the chelated complex in the presence of pyridine (Figure 1). Brown block crystals suitable for X-ray diffraction analysis were harvested. Yield (0.0455 g, 75%). ¹H NMR (500 MHz, DMSO-*d*₆) δ 8.86–8.83 (m, 2H), 8.58 (d, *J* = 7.2 Hz, 1H), 8.30 (d, *J* = 7.7 Hz, 1H), 8.17–8.14 (m, 1H), 7.94–7.91 (m, 1H), 7.85–7.83 (m, 1H), 7.43–7.40 (m, 1H). ¹³C NMR (125 MHz, DMSO-*d*₆) δ 182.8, 182.3, 147.5, 144.0, 137.5, 134.3, 134.2, 131.1, 130.6, 129.7, 128.1, 127.0, 125.4, 124.9, 122.3, 121.4, 40.4. ESI-MS *m/z*: 497.9 [M - DMSO + Cl]⁻. IR (KBr): 3474, 3071, 3000, 2912, 1659, 1515, 1585, 1564, 1226, 1124, 1291, 1032, 1017, 979, 941, 785, 720, 685, 650 cm⁻¹. Elemental analysis calcd (%) for C₁₈H₁₄ClNO₂PtS: C 40.12, H 2.62, N 2.60. Found: C 40.35, H 2.75, N 2.55.

Synthesis of 6-Hydroxyoxoisoaporphine Alkaloid (L^b) and Pt2. A mixture of phthalic anhydride (30 g, 0.2 mol) and 4-bromine phenylethylamine (40.5 g, 0.2 mol) in anhydrous ethanol was refluxed for 6 h. After cooling to 0–5 °C, the formed crystals of 4-bromophenylethylphthalimide (49.5 g, 75%) were filtered and washed with ethanol. The product was pure enough for the next reaction.

To a mixture of anhydrous aluminum chloride (75 g, 0.56 mol) and sodium chloride (15 g, 0.26 mol), 4-bromophenylethylphthalimide (33 g, 0.1 mol) was slowly added at 180 °C for 30 min. The reaction was allowed to continue at 220–230 °C for 3.5 h. The product was cooled, finely ground, and poured slowly into concentrated sulfuric acid (650 mL) at 90 °C. The mixture was stirred and heated at 230–240 °C for 3.5 h. After being cooled, the solution was placed on ice. Sodium hydroxide was added until pH 2–3 was obtained, and the resultant precipitate was filtered and washed in turn with dilute aqueous sodium hydroxide and water to give the crude product 6-bromine-oxoisoaporphine, which was extracted with acetic acid.

The extract was condensed under reduced pressure, and the resultant precipitate was washed, dried, and sublimed at 130–140 °C at a pressure of 1 mmHg to give the 6-bromine-oxoisoaporphine (9.55

g, 31%) as a light yellow solid. The crystal of 6-bromine-oxoisoporphine was prepared in methanol under solvothermal conditions. $^1\text{H NMR}$ (500 MHz, CDCl_3 - d_1) δ 8.94 (d, $J = 7.9$ Hz, 1H, 2-H-Ar), 8.82 (d, $J = 5.6$ Hz, 1H, 11-H-Ar), 8.60 (s, 1H, 4-H-Ar), 8.44 (d, $J = 7.7$ Hz, 1H, 8-H-Ar), 8.16 (s, 1H, 5-H-Ar), 7.86 (t, $J = 7.5$ Hz, 1H, 10-H-Ar), 7.70 (m, 2H, 8-H-Ar and 9-H-Ar). IR (KBr): 3060, 1667, 1595, 1396, 1283, 1190, 1092, 897, 705, 642, 595 cm^{-1} .

To a stirred refluxing suspension of 6-bromine-oxoisoporphine (3.1 g, 0.01 mol) in 80 mL of EtOH/ H_2O (5:3), NaOH (4.0 g, 0.1 mol) was added. The mixture was stirred at reflux for 12 h, cooled to room temperature, filtered, and washed with ether and water. The crude solid was purified by column chromatography with petroleum ether/ethyl acetate (100:1) elution to afford a yellow solid 6-hydroxyloxoisoisoporphine alkaloid (L^b) (1.24 g, 50%). $^1\text{H NMR}$ (500 MHz, $\text{DMSO}-d_6$) δ 15.01 (s, 1H), 8.88 (d, $J = 8.0$ Hz, 1H), 8.80 (d, $J = 5.2$ Hz, 1H), 8.38 (d, $J = 9.1$ Hz, 1H), 8.35 (d, $J = 7.9$ Hz, 1H), 8.00 (d, $J = 5.2$ Hz, 1H), 7.96–7.94 (m, 1H), 7.80–7.77 (m, 1H), 7.57 (d, $J = 9.1$ Hz, 1H). $^{13}\text{C NMR}$ (125 MHz, $\text{DMSO}-d_6$) δ 186.1, 168.5, 144.0, 143.8, 139.7, 136.7, 134.8, 130.7, 130.5, 123.0, 126.6, 125.2, 122.6, 121.2, 108.1. ESI-MS m/z : 473.0 [$\text{M} - 2\text{Cl} + \text{CH}_3\text{OH}$] $^+$. IR (KBr): 3423, 3065, 2950, 1636, 1657, 1448, 1423, 1380, 1352, 1267, 1242, 1163, 1141, 889, 852, 790, 754, 729, 589, 551 cm^{-1} . Elemental analysis calcd (%) for $\text{C}_{16}\text{H}_9\text{NO}_2$: C 77.72, H 3.67, N 5.67. Found: C 77.65, H 3.58, N 5.74.

The complex $[\text{PtL}^b(\text{DMSO})\text{Cl}]$ (Pt_2) was prepared by treating L^b (0.0246 g, 0.1 mM) with $\text{Pt}(\text{DMSO})_2\text{Cl}_2$ (0.0422 g, 0.1 mM) in methanol/water (25:1) under solvothermal conditions. L^b deprotonation took place upon the addition of $\text{Pt}(\text{II})$ ion to the ligand solution to form the complex in the presence of pyridine (Figure 1). Brown block crystals suitable for X-ray diffraction analysis were harvested. Yield (0.0499 g, 90%). $^1\text{H NMR}$ (500 MHz, $\text{DMSO}-d_6$) δ 14.57 (s, 1H), 9.01 (d, $J = 7.8$ Hz, 1H), 8.91 (d, $J = 5.2$ Hz, 1H), 8.56 (d, $J = 7.6$ Hz, 1H), 8.14 (m, 2H), 7.85 (t, $J = 7.5$ Hz, 1H), 7.50 (t, $J = 7.5$ Hz, 1H). ESI-MS m/z : 473.0 [$\text{M} - \text{DMSO} - \text{Cl} + \text{CH}_3\text{OH}$] $^+$. IR (KBr): 3418, 2972, 2923, 1626, 1602, 1563, 1476, 1421, 1382, 1256, 1223, 1086, 1045, 990, 877, 847, 806, 790, 738 cm^{-1} . Elemental analysis calcd (%) for $\text{C}_{18}\text{H}_{14}\text{ClNO}_3\text{PtS}$: C 38.96, H 2.54, N 2.52. Found: C 38.83, H 2.43, N 2.58.

X-ray Crystallography. The data collection of single crystals of L^b and Pt_1 and Pt_2 was performed on a SuperNova CCD diffractometer equipped with graphite monochromated Mo $K\alpha$ radiation ($\lambda = 0.71073$ Å) at room temperature. The structures were solved with direct methods and refined using SHELX-97 programs.⁵⁰ The non-hydrogen atoms were located in successive difference Fourier synthesis. The final refinement was performed by full-matrix least-squares methods with anisotropic thermal parameters for non-hydrogen atoms on F^2 . The hydrogen atoms were added theoretically and riding on the concerned atoms. The parameters used intensity collection and refinements are summarized in Tables S1 and S2 together with the crystal data.

Cytotoxicity Assay and Cellular Morphology. The cell culture was maintained in RPMI-1640 medium supplemented with 10% fetal bovine serum (FBS), 100 U/mL penicillin, and 100 $\mu\text{g}/\text{mL}$ streptomycin in 25 cm^2 culture flasks at 37 °C in a humidified atmosphere with 5% CO_2 . All cells to be tested in the following assays had a passage number of 3–6.

T-24, HepG2, SK-OV-3, SK-OV-3/DDP, BEL-7404, NCI-H460, HCT-8, and HL-7702 cells were seeded in 96-well plates [(5.0 \times 10³)/180 μL]/well). Cells were grown for 12 h to reach 70% confluence before treatment, and an amount of 20 μL of tested various concentrations of compounds was added to each well. The final concentrations of the tested compounds were 1.25, 2.5, 5.0, 10.0, and 20.0 μM , respectively. The resultant solutions were subsequently added to a set of wells. Control wells contained media with 0.5% DMSO. The microtiter plates were incubated at 37 °C in a humidified atmosphere of 5% CO_2 /95% air for another 2 days. At the end of each incubation period, the 3-(4,5-dimethylthiazol-2-yl)-2,5-diphenyltetrazolium bromide (MTT) solution (10 μL , 5 mg/mL) was added to each well, and the cultures were incubated further for 6 h at 37 °C in a

humidified atmosphere of 5% CO_2 /95% air. After removal of the supernatant, DMSO (100 μL) was added to dissolve the formazan crystals. The absorbance was read on a microplate reader at 490/630 nm. The cytotoxicity was evaluated based on the percentage of cell survival compared with the negative control. The final IC_{50} values were calculated by the Bliss method ($n = 5$). All tests were repeated in at least three independent trials.

Uptake of Platinum Complexes in Cells. SK-OV-3/DDP cells (~10 million cells) were treated with 10 μM Pt_1 and Pt_2 , respectively, for 8 h at 37 °C in a humidified 5% CO_2 incubator. The medium was then removed, and the cells were washed with 5 mL of PBS, scraped, and collected in 5 mL of PBS. The scrapped cells were collected by centrifuging at 2500 rpm for 10 min. The obtained cell pellet was dissolved in 1 M NaOH (1 mL) and diluted with 2% (v/v) HNO_3 (5 mL) for determining the whole cell platinum content. Another set was treated similarly to isolate nuclear fraction, nuclear proteins, membrane proteins, and cytoplasmic protein as described by Schreiber et al.²⁶ The final solution was made up to 5 mL using 2% (v/v) HNO_3 , and the amount of platinum taken up by the cells was determined by ICP-MS. The instrument was calibrated for platinum using standard solutions containing 10, 50, 100, 500, and 1000 ppb platinum.

Confocal Morphological Examination. The AO/EB molecular probes were used to detect apoptotic cells.²⁷ To examine whether Pt_1 and Pt_2 induce apoptosis in SK-OV-3/DDP cell line, cells were plated in six-well plates and treated with 5.0 μM Pt_1 and Pt_2 for 12 h, respectively. The cells were then trypsinized, harvested, suspended in PBS, stained with 100 $\mu\text{g}/\text{mL}$ AO and 100 $\mu\text{g}/\text{mL}$ EB for 10 min at room temperature, respectively, and visualized immediately by confocal microscopy (CarlZeiss LSM 710, Germany) with excitation wavelength of 488 nm (AO) or 510 nm (EB). Apoptotic cells were defined based on the nuclear morphology changes such as chromatin condensation and fragmentation.

Fluorescence Morphological Examination. To examine whether Pt_1 and Pt_2 induce apoptosis in SK-OV-3/DDP cancer cells, the cells were plated in six-well plates and treated with 5, 10, and 20 μM Pt_1 and Pt_2 for 12 h, respectively. After the treatment, the cells were washed with PBS and fixed for 10 min at room temperature. The cells were rinsed twice in PBS and stained with a fluorescent dye, Hoechst 33258 fluorescent dye (Beyotime, China), at room temperature in the dark for 10 min. The cells were then washed twice with PBS, examined, and immediately photographed under a fluorescent microscope (Nikon Te2000, Japan) with excitation wavelength of 330–380 nm. Apoptotic cells were defined on the basis of nuclear morphology changes such as chromatin condensation and fragmentation.

SA- β -Gal Assay. After long-term culture of cells with Pt_1 and Pt_2 , the growth medium was aspirated, and the cells were fixed in 2% formaldehyde/0.2% glutaraldehyde for 15 min at room temperature. The fixing solution was removed; the cells were gently washed twice with PBS and then stained using β -Gal staining solution containing 1 mg/mL 5-bromo-4-chloro-3-indolyl- β -D-galactoside overnight at 37 °C. The staining solution was removed, and the cells were washed three times with PBS and viewed under an optical microscope and photographed (Nikon Te2000, Japan).

Flow Cytometric Analysis. In cell cycle analysis, the SK-OV-3/DDP cells were maintained with 10% fetal calf serum in 5% CO_2 at 37 °C. Cells were harvested by trypsinization and rinsed with PBS. After centrifugation, the pellet (10⁵–10⁶ cells) was suspended in 1 mL of PBS and then fixed by dropwise addition of 9 mL of precooled (4 °C) 70% ethanol under violent shaking. After treatment, cells were collected and fixed with ice-cold 70% ethanol at –20 °C overnight. Fixed cells were resuspended in 0.5 mL of PBS containing 50 $\mu\text{g}/\text{mL}$ propidium iodide and 100 $\mu\text{g}/\text{mL}$ RNase A. The cell cycle distribution was analyzed by FACS Calibur flow cytometer (BD) and calculated using ModFIT LT software (BD).

Apoptosis Analysis. Apoptosis was detected by flow cytometric analysis of annexin V staining. Annexin V-FITC/PI assay was performed as previously described.⁵¹ Briefly, adherent SK-OV-3/DDP cells were harvested and suspended in the annexin-binding buffer (5 \times 10⁵ cells/mL). Then cells were incubated with annexin V-FITC

and PI for 1 h at room temperature in the dark and immediately analyzed by flow cytometry. The data are presented as biparametric dot plots showing PI red fluorescence vs annexin V-FITC green fluorescence.

Immunofluorescence. SK-OV-3/DDP cells were grown on polylysine-coated coverslips, rinsed in phosphate-buffered saline, fixed in cold methanol for 20 min, permeabilized for 10 min in 0.5% Triton X-100 on ice, and blocked in 5% BSA for 30 min at room temperature. The coverslips were incubated with rabbit monoclonal anti-53BP1, mouse monoclonal anti-TRF1 and anti-TRF2 (Abcam) primary antibodies for 3.0 h at 25 °C. The coverslips were washed and incubated with fluorescein conjugated goat anti-mouse (1:1000) and rhodamine conjugated goat anti-mouse (1:1000) secondary antibodies. Finally, the cells stained with 0.1 mg/mL DAPI. Fluorescence images were captured using confocal microscopy (CarlZeiss LSM 710, Germany).

Determination of Caspase-3 and Caspase-9 Activity by Flow Cytometric Analysis. The measurement of caspase-3 and caspase-9 activity was performed by CaspGLOW fluorescein active caspase-3 and caspase-9 staining kit. After treatment with 10.0 μ M Pt1 and Pt2 for 8 h, respectively, the cells in RPMI 1640 medium with 10% FBS at a density of 1×10^6 cells/mL were harvested, washed with PBS three times, and then resuspended in 300 μ L volume; 1 μ L of FITC-DEVD-FMK or FITC-LEHD-FMK was consequently added and incubated for 1.0 h at 37 °C in 5% CO₂ incubator. The cells were then examined by a FACSAria II flow cytometer equipped with a 488 nm argon laser. The results were represented as the percent change on the activity comparing with the control.

Measurement of Mitochondrial Membrane Potential. The loss of mitochondrial membrane potential ($\Delta\psi$) was assessed using a lipophilic cationic fluorescent probe, JC-1 (5,5',6,6'-tetrachloro-1,1',3,3'-tetraethylbenzimidazolylcarbocyanine; Beyotime). Cells treated with 5.0, 10.0, and 20.0 μ M Pt1 and Pt2 for 12 h were incubated with 5 μ g/mL JC-1 for 20 min at 37 °C and examined by fluorescence microscopy. The emission fluorescence for JC-1 was monitored at 530 and 590 nm, under the excitation wavelength at 488 nm. The orange-red emission of the dye is attributable to a potential-dependent aggregation in the mitochondria, which reflects the $\Delta\psi$. Green fluorescence reflects the monomeric form of JC-1, appearing in the cytosol after mitochondrial membrane depolarization.

Spectral Studies of Interactions with GSH. The UV/vis spectroscopic titrations were carried out at room temperature by adding increasing amounts of GSH (0, 2.0×10^{-5} , 4.0×10^{-5} , 6.0×10^{-5} , 8.0×10^{-5} , 1.0×10^{-4} , 1.2×10^{-4} , and 1.4×10^{-4} M, respectively) to a solution of Pt1 or Pt2 at a fixed concentration (2.0×10^{-5} M) contained in a quartz cell. The time span between two successive spectra was 10 min.

Protein Binding Studies. All the experiments involving the binding of the complex with BSA were carried out in double distilled water with trisodium citrate (Tris, 10 mM) and sodium chloride (100 mM) and adjusted to pH 7.35 with hydrochloric acid. The 1×10^{-3} M BSA stock solution was stored at 4 °C for no more than 5 days before use. Pt1 and Pt2 were both prepared as 1×10^{-3} M DMSO stock solutions for protein binding studies.

The solution of 5.0×10^{-7} M BSA was distilled by adding 1.5 μ L of 1×10^{-3} M BSA in buffer (100 mM NaCl and 10 mM trisodium citrate at pH 7.35). The binding of the protein with the complex was studied by adding a certain amount of a solution of the complex stepwise (0–8 μ M) into the solution of 5.0×10^{-7} M BSA. The emission spectra were monitored by keeping the excitation of BSA at 280 nm, and the emission was monitored in the range of 290–450 nm. The slit width was set as 5 nm/5 nm for E_x/E_m , respectively, and the emission was observed at 345 nm.

Commonly, fluorescence quenching can be described by the following Stern–Volmer equation.⁵²

$$F_0/F = 1 + k_q\tau_0[Q] = 1 + K_{SV}[Q]$$

where F_0 and F are the steady-state fluorescence intensities in the absence and presence of quencher, respectively; K_{SV} is the Stern–Volmer quenching constant, obtained from the slope of the plot F_0/F

vs complex concentration; $[Q]$ is the total concentration of quencher; K_q is the bimolecular quenching constant; and τ_0 is the average lifetime of protein in the absence of quencher (its value is 10^{-8} s).

Telomerase Inhibition (TRAP Assay). A total of 5×10^6 tumor cells untreated or treated with compound were pelleted and lysed for 30 min on ice. The lysate was centrifuged at 13 000 rpm for 30 min at 4 °C; the supernatant was collected and stored at –80 °C before use. Telomerase inhibition efficiency of the compound was measured by telomeric repeat amplification protocol enzyme-linked immunosorbent assay (TRAP-ELISA).⁵³ The procedure was the same as for the TRAP assay. The telomerase product was detected using an enzyme-linked probe. Absorbance read by the microplate reader was reported as A_{450nm} against the blank (reference, A_{690nm}). For RNase treatment, the maximum value of absorbance for the negative control (2.5 μ L of the corresponding RNase-treated or heated cell extract) should be lower than $0.25(A_{450nm} - A_{690nm})$ units. The absorbance for the positive control examined in 30 min reaction (cell extract was prepared from the immortalized telomerase-expressing human kidney cells, and lyophilizate extract was supplied with the kit) should be higher than $1.5(A_{450nm} - A_{690nm})$ units.

RNA Extraction. Cell pellets harvested from each well of the culture plates were lysed in RZ lysis solution. RNA was extracted with RNAsimple total RNA kit (TIANGEN) according to manufacturer's protocol and eluted in distilled, deionized water with 0.1% diethyl pyrocarbonate (DEPC) to a final volume of 50 μ L. RNA was stored at –80 °C before use.

Reverse Transcription Polymerase Chain Reaction (RT-PCR). Total RNA was used as the template for reverse transcription using the following protocol: each 20 μ L reaction contained 2.0 μ L of 10 \times RT mix, 2.0 μ L of dNTP (2.5 mM), 2.0 μ L of oligo-dT15 primer, 1.0 μ L of Quant reverse transcriptase, 10 μ L of DEPC-H₂O, and 2 μ g of total RNA. The mixture was incubated at 37 °C for 60 min and then immediately placed on ice. The synthesized cDNA was stored at –80 °C. Real-time PCR was performed on 7500 fast RealTime PCR (ABI Co. Ltd., USA) by using 2.5 \times Real Master Mix/20 \times SYBR solution (TIANGEN), according to the manufacturer's protocol. The primer sequences are shown in Table 4 (c-myc, hTERT, bcl-2, and GAPGH). The total volume of 20 μ L of real-time RT-PCR reaction mixtures contained 9.0 μ L of 2.5 \times Real Master Mix/20 \times SYBR solution, 0.25 μ M each of forward and reverse primers, 1.0 μ L of cDNA, and nuclease-free water. The program used for all genes consisted of a denaturing cycle of 3 min at 95 °C, 45 cycles of PCR (95 °C for 20 s, 58 °C for 30 s, and 68 °C for 30 s), a melting cycle consisting of 95 °C for 15 s, 65 °C for 15 s, and a step cycle starting at 65 °C with a 0.2 °C/s transition rate to 95 °C. The specificity of the real-time RT-PCR product was confirmed by melting curve analysis. The PCR product sizes were confirmed by agarose gel electrophoresis and ethidium bromide staining. Three replications were performed, and the bcl-2 mRNA, hTERT mRNA or c-myc mRNA level was normalized against GAPDH mRNA level for each sample. Results of real-time PCR were analyzed using the $2^{-\Delta\Delta CT}$ method in the program Origin 8.0 to compare the transcriptional levels of bcl-2, hTERT or c-myc genes in each sample relative to untreated control.

Western Blot. Cells harvested from each well of the culture plates were lysed in 150 μ L of extraction buffer consisting of 149 μ L of RIPA lysis buffer and 1 μ L of PMSF (100 mM). The suspension was centrifuged at 10 000 rpm at 4 °C for 10 min, and the supernatant (10 μ L for each sample) was loaded onto 10% polyacrylamide gel and then transferred to a microporous polyvinylidene difluoride (PVDF) membrane. Western blotting was performed using anti-bcl-2, anti-hTERT, anti-c-myc, anti-53BP1, anti-TRF1, anti-TRF2, or anti- β -actin primary antibody and horseradish-peroxidase-conjugated anti-mouse or anti-rabbit secondary antibody. The protein bands were visualized using chemiluminescence substrate.

Transfection. SK-OV-3/DDP cells (8.0×10^5) were grown in 3 cm Petri dishes, and after 24 h, DNA transfections were performed as follows. First, 2.0 μ g of EGFP plasmid⁴¹ or 2.0 μ g c-myc plasmid⁴² were co-transfected into cells using Lipofectamine 2000 (Invitrogen). Then, Pt1 and Pt2 were added into medium after 6 h of transfection. After another 24 h of drug treatment, the cells were

imaged using Nikon TE2000 (Japan) scanning fluorescent microscope and studied by luciferase reporter gene assay kit.

In Vivo Antitumor Activity toward HCT-8 and NCI-H460 Human Tumor. The in vivo antitumor studies were carried out at the Institute of Biomedical Engineering of the Chinese Academy of Medical Sciences (Tianjin, China). The handling of animals and the experimental design were approved by the Ethics Committee and Animal Care Committee of the Institute. Six-week-old athymic BALB/cA nu/nu female mice (18–20 g for NCI-H460 model) were purchased from the Institute of Laboratory Animal Resources of National Institutes for Food and Drug Control of China (Beijing). Animals were housed in a sterile environment with conditions of constant photoperiod (12 h light/12 h dark at 23–24 °C and 65–85% humidity). HCT-8 and NCI-H460 cells were harvested and injected subcutaneously into the right flank (5×10^6 cells in 200 μ L of serum-free medium).

When the xenograft tumor grew to a volume of about 1000 mm³, the mice were sacrificed, and the tumor tissues were cut into about 1.5 mm³ small pieces, which were then transplanted into the right flank of female nude mice. When tumors reached a volume of 100–300 mm³ in all mice, the mice were randomized into vehicle control and treatment groups ($n = 6$ –7/group). In HCT-8 xenograft model, mice received the following treatments: (a) control, 5% v/v DMSO/saline vehicle, (b) Pt1 at 6 and 3 mg/kg per 2 days (5% DMSO in saline, v/v), (c) Pt2 at 6 and 3 mg/kg per 2 days (5% DMSO in saline, v/v), (d) cisplatin at 2 mg/kg per 2 days (dissolved in saline), used as a positive comparison. While in the NCI-H460 xenograft model, mice were treated with Pt1 and Pt2 at 6 mg/kg per 2 days. All mice were sacrificed after 16 days of treatment, and the tumor weight was recorded.

The tumor volumes were determined every 3 days by measuring length (l) and width (w) and calculating volume ($V = lw^2/2$) as described elsewhere.⁵⁴ Meanwhile, the body weight was measured and taken as a parameter of systemic toxicity. The rate of tumor growth was calculated using the following formula: tumor growth = $(1 - TW_c/TW_t) \times 100$, where TW_t is the tumor weight in complex-treated mice and the TW_c is the tumor weight in vehicle-treated animals.⁵⁵

Statistical Analysis. The experiments have been repeated from three to five times, and the results obtained are presented as the mean \pm standard deviation (SD). Significant changes were assessed by using Student's t test for unpaired data, and p values of <0.05 were considered statistically significant.

■ ASSOCIATED CONTENT

● Supporting Information

Vendor codes for each tested compound, thermal stability experiments, UV–vis, fluorescence, CD spectra, ¹H NMR, ¹³C NMR, ESI-MS, IR, and HPLC data, crystal data (CCDC No.: 1017916–1017918), results from safety assessment of **1** and **2** in vivo, and growth inhibition of HCT-8 and H460 xenograft in vivo. This material is available free of charge via the Internet at <http://pubs.acs.org>.

■ AUTHOR INFORMATION

Corresponding Authors

*Z.-F.C.: telephone, 086-773-2120998; fax, 086-773-21209958; e-mail, chenzxf@gxnu.edu.cn; Hong Liang, PhD Telephone:

*H.L.: telephone, 086-773-2120958; fax, 086-773-21209958; e-mail, hliang@gxnu.edu.cn.

Notes

The authors declare no competing financial interest.

■ ACKNOWLEDGMENTS

This work was supported by the National Natural Science Foundation of China (Grants 21271051, 81473102, 21431001), National Basic Research Program of China (Grant 2012CB723501), IRT1225, CMEMR2012-A22, and

Natural Science Foundation of Guangxi Province (Grants 2012GXNSFDA053005 and 2012GXNSFDA385001) as well as “BAGUI Scholar” program of Guangxi Province of China.

■ ABBREVIATIONS USED

FID, fluorescent intercalator displacement; G4, G-quadruplex; TO, thiazole orange; T_m , melting temperature; SD, standard deviation; FRET, fluorescence resonance energy transfer; PI, propidium iodide; TGI, tumor growth inhibition; IR, tumor growth inhibition rate

■ REFERENCES

- (1) (a) Kim, N. W.; Piatyszek, M. A.; Prowse, K. R.; Harley, C. B.; West, M. D.; Ho, P. L.; Coviello, G. M.; Wright, W. E.; Weinrich, S. L.; Shay, J. W. Specific association of human telomerase activity with immortal cells and cancer. *Science* **1994**, *266*, 2011–2015. (b) Huffman, K. E.; Levene, S. D.; Tesmer, V. M.; Shay, J. W.; Wright, W. E. Telomere shortening is proportional to the size of the G-rich telomeric 3'-overhang. *J. Biol. Chem.* **2000**, *275*, 19719–19722. (c) Wright, W. E.; Tesmer, V. M.; Huffman, K. E.; Levene, S. D.; Shay, J. W. Normal human chromosomes have long G-rich telomeric overhangs at one end. *Genes Dev.* **1997**, *11*, 2801–2809. (d) McElligott, R.; Wellinger, R. J. The terminal DNA structure of mammalian chromosomes. *EMBO J.* **1997**, *16*, 3705–3714.
- (2) (a) Biffi, G.; Tannahill, D.; McCafferty, J.; Balasubramanian, S. Quantitative visualization of DNA G-quadruplex structures in human cells. *Nat. Chem.* **2013**, *5*, 182–186. (b) Siddiqui-Jain, A.; Hurley, L. H. DNA structure: visualizing the quadruplex. *Nat. Chem.* **2013**, *5*, 153–155. (c) Paeschke, K.; Simonsson, T.; Postberg, J.; Rhodes, D.; Lipps, H. J. Telomere end-binding proteins control the formation of G-quadruplex DNA structures in vivo. *Nat. Struct. Mol. Biol.* **2005**, *12*, 847–854. (d) Lam, E. Y. N.; Beraldi, D.; Tannahill, D.; Balasubramanian, S. G-quadruplex structures are stable and detectable in human genomic DNA. *Nat. Commun.* **2013**, *4*, 1796 DOI: 10.1038/ncomms2792. (e) Xu, Y.; Komiyama, M. Evidence for G-quadruplex DNA in human cells. *ChemBioChem* **2013**, *14*, 927–928.
- (3) (a) De Cian, A.; Lacroix, L.; Douarre, C.; Temime-Smaali, N.; Trentesaux, C.; Riou, J.-F.; Mergny, J.-L. Targeting telomeres and telomerase. *Biochimie* **2008**, *90*, 131–155. (b) Mocellin, S.; Pooley, K. A.; Nitti, D. Telomerase and the search for the end of cancer. *Trends Mol. Med.* **2013**, *19*, 125–133. (c) Ruden, M.; Puri, N. Anti-tumour treatment: novel anticancer therapeutics targeting telomerase. *Cancer Treat. Rev.* **2013**, *39*, 444–456.
- (4) Riou, J. F.; Guittat, L.; Mailliet, P.; Laoui, A.; Renou, E.; Petitgenet, O.; Megnin-Chanet, F.; Helene, C.; Mergny, J. L. Cell senescence and telomere shortening induced by a new series of specific G-quadruplex DNA ligands. *Proc. Natl. Acad. Sci. U.S.A.* **2002**, *99*, 2672–2677.
- (5) (a) McEachern, M. J.; Krauskopf, A.; Blackburn, E. H. Telomeres and their control. *Annu. Rev. Genet.* **2000**, *34*, 331–358. (b) Shay, J. W.; Wright, W. E. Telomerase therapeutics for cancer: challenges and new directions. *Nat. Rev. Drug Discovery* **2006**, *5*, 577–584. (c) Kelland, L. R. Overcoming the immortality of tumour cells by telomere and telomerase based cancer therapeutics—current status and future prospects. *Eur. J. Cancer.* **2005**, *41*, 971–979. (d) Pendino, F.; Tarkanyi, I.; Dudognon, C.; Hillion, J.; Lanotte, M.; Aradi, J.; Segal-Bendirdjian, E. Telomeres and telomerase: pharmacological targets for new anticancer strategies? *Curr. Cancer Drug Targets* **2006**, *6*, 147–180. (e) Brassart, B.; Gomez, D.; Decan Cian, A.; Paterski, R.; Montagnac, A.; Qui, K.-H.; Temime-Smaali, N.; Trentesaux, C.; Mergny, J.-L.; Gueritte, F.; Riou, J.-F. A new steroid derivative stabilizes G-quadruplexes and induces telomere uncapping in human tumor cells. *Mol. Pharmacol.* **2007**, *72*, 631–640.
- (6) (a) Zahler, A. M.; Williamson, J. R.; Cech, T. R.; Prescott, D. M. Inhibition of telomerase by G-quartet DNA structures. *Nature* **1991**, *350*, 718–720. (b) Sun, D.; Thompson, B.; Cathers, B. E.; Salazar, M.; Kerwin, S. M.; Trent, J. O.; Jenkins, T. C.; Neidle, S.; Hurley, L. H. Inhibition of human telomerase by a G-quadruplex-interactive

- compound. *J. Med. Chem.* **1997**, *40*, 2113–2116. (c) Neidle, S. Human telomeric G-quadruplex: the current status of telomeric G-quadruplexes as therapeutic targets in human cancer. *FEBS J.* **2010**, *277*, 1118–1125.
- (7) (a) Phan, A. T.; Kuryavyi, V.; Gaw, H. Y.; Patel, D. J. Small-molecule interaction with a five-guanine-tract G-quadruplex structure from the human MYC promoter. *Nat. Chem. Biol.* **2005**, *1*, 167–173. (b) Phan, A. T.; Kuryavyi, V.; Burge, S.; Neidle, S.; Patel, D. J. Structure of an unprecedented G-quadruplex scaffold in the human c-kit promoter. *J. Am. Chem. Soc.* **2007**, *129*, 4386–4392. (c) Shirude, P. S.; Okoumus, B.; Ying, L.; Ha, T.; Balasubramanian, S. Single-molecule conformational analysis of G-quadruplex formation in the promoter DNA duplex of the proto-oncogene C-Kit. *J. Am. Chem. Soc.* **2007**, *129*, 7484–7485. (d) Todd, A. K.; Haider, S. M.; Parkinson, G. N.; Neidle, S. Sequence occurrence and structural uniqueness of a G-quadruplex in the human c-kit promoter. *Nucleic Acids Res.* **2007**, *35*, 5799–5808. (e) Dai, J.; Dexheimer, T. S.; Chen, D.; Carver, M.; Ambrus, A.; Jones, R. A.; Yang, D. An intramolecular G-quadruplex structure with mixed parallel/antiparallel G-strands formed in the human BCL-2 promoter region in solution. *J. Am. Chem. Soc.* **2006**, *128*, 1096–1098. (f) Dexheimer, T. S.; Sun, D.; Hurley, L. H. Deconvoluting the structural and drug-recognition complexity of the G-quadruplex-forming region upstream of the bcl-2 P1 promoter. *J. Am. Chem. Soc.* **2006**, *128*, 5404–5415. (g) Yuan, L.; Tian, T.; Chen, Y.; Yan, S.; Xing, X.; Zhang, Z.; Zhai, Q.; Xu, L.; Wang, S.; Weng, X.; Yuna, B.; Feng, Y.; Zhou, X. Existence of G-quadruplex structures in promoter region of oncogenes confirmed by G-quadruplex DNA cross-linking strategy. *Sci. Rep.* **2013**, *3*, 1811.
- (8) Ou, T.-M.; Lu, Y.-J.; Tan, J.-H.; Huang, Z.-S.; Wong, K.-Y.; Gu, L.-Q. G-quadruplexes: Targets in anticancer drug design. *ChemMedChem* **2008**, *3*, 690–713.
- (9) Flores, I.; Eevan, G.; Blasco, M. A. Genetic analysis of myc and telomerase interactions in vivo. *Mol. Cell. Biol.* **2006**, *26*, 6130–6138.
- (10) Camarena, F. S.; Serral, G. C.; Santalo, F. S. Telomerase and telomere dynamics in ageing and cancer: current status and future directions. *Transl. Oncol.* **2007**, *9*, 145–154.
- (11) Wang, X.-D.; Ou, T.-M.; Lu, Y.-J.; Li, Z.; Xu, Z.; Xi, C.; Tan, J.-H.; Huang, S.-L.; An, L.-K.; Li, D.; Gu, L.-Q.; Huang, Z.-S. Turning off transcription of the bcl-2 gene by stabilizing the bcl-2 promoter quadruplex with quindoline derivatives. *J. Med. Chem.* **2010**, *53*, 4390–4398.
- (12) (a) Neidle, S. P.; Parkinson, G. N. Quadruplex DNA crystal structures and drug design. *Biochimie* **2008**, *90*, 1184–1196. (b) Balasubramanian, S. H.; Hurley, L. H.; Neidle, S. Targeting G-quadruplexes in gene promoters: a novel anticancer strategy? *Nat. Rev. Drug Discovery* **2011**, *10*, 261–275.
- (13) (a) Rezler, E. M.; Bearss, D. J.; Hurley, L. H. Telomere inhibition and telomere disruption as processes for drug targeting. *Annu. Rev. Pharmacol. Toxicol.* **2003**, *43*, 359–379. (b) Fu, B.; Huang, J.; Ren, L.; Weng, X.; Zhou, Y.; Du, Y.; Wu, X.; Zhou, X.; Yang, G. Cationic corrole derivatives: a new family of G-quadruplex inducing and stabilizing ligands. *Chem. Commun.* **2007**, 3264–3266. (c) Xu, Y. Chemistry in human telomere biology: structure, function and targeting of telomere DNA/RNA. *Chem. Soc. Rev.* **2011**, *40*, 2719–2740. (d) Maji, B.; Kumar, K.; Kaulage, M.; Muniyappa, K.; Bhattacharya, S. Design and synthesis of new benzimidazole-carbazole conjugates for the stabilization of human telomeric DNA, telomerase inhibition, and their selective action on cancer cells. *J. Med. Chem.* **2014**, *57*, 6973–6988. (e) Laguerre, A.; Stefan, L.; Larrouy, M.; Genest, D.; Novotna, J.; Pirrotta, M.; Monchaud, D. A twice-as smart synthetic G-quartet: PyroTASQ is both a smart quadruplex ligand and a smart fluorescent probe. *J. Am. Chem. Soc.* **2014**, *136*, 12406–12414.
- (14) (a) Sekaran, V.; Soares, J.; Jarstfer, M. B. Telomere maintenance as a target for drug discovery. *J. Med. Chem.* **2014**, *57*, 521–538. (b) Micco, M.; Collie, G. W.; Dale, A. G.; Ohnmacht, S. A.; Pazitna, I.; Gunaratnam, M.; Reszka, A. P.; Neidle, S. Structure-based design and evaluation of naphthalene diimide G-quadruplex ligands as telomere targeting agents in pancreatic cancer cells. *J. Med. Chem.* **2013**, *56*, 2959–2974. (c) Leva, F. S. D.; Zizza, P.; Cingolani, C.; D'Angelo, C.; Pagano, B.; Amato, J.; Salvati, E.; Sissi, C.; Pinato, O.; Marinelli, L.; Cavalli, A.; Cosconati, S.; Novellino, E.; Randazzo, A.; Biroccio, A. Exploring the chemical space of G-quadruplex binders: discovery of a novel chemotype targeting the human telomeric sequence. *J. Med. Chem.* **2013**, *56*, 9646–9654. (d) Chen, H.; Long, H.; Cui, X.; Zhou, J.; Xu, M.; Yuan, G. Exploring the formation and recognition of an important G-quadruplex in a HIF1 α promoter and its transcriptional inhibition by a benzo[c]phenanthridine derivatives. *J. Am. Chem. Soc.* **2014**, *136*, 2583–2591. (e) Wang, X.; Zhou, C.-L.; Yan, J.-W.; Hou, J.-Q.; Chen, S.-B.; Ou, T.-M.; Gu, L.-Q.; Huang, Z.-S.; Tan, J.-H. Synthesis and evaluation of quinazolone derivatives as a new class of c-KIT G-quadruplex binding ligands. *ACS Med. Chem. Lett.* **2013**, *4*, 909–914. (f) Lu, Y.-J.; Ou, T.-M.; Tan, J.-H.; Hou, J.-Q.; Shao, W.-Y.; Peng, D.; Sun, N.; Wang, X.-D.; Wu, W.-B.; Bu, X.-Z.; Huang, Z.-S.; Ma, D.-L.; Wong, K.-Y.; Gu, L.-Q. 5-N-methylated quindoline derivatives as telomeric G-quadruplex stabilizing ligands: effects of 5-N-positive charge on quadruplex binding affinity and cell proliferation. *J. Med. Chem.* **2008**, *51*, 6381–6397.
- (15) (a) Ou, T.-M.; Lu, Y.-J.; Zhang, C.; Huang, Z.-S.; Wang, X.-D.; Tan, J.-H.; Chen, Y.; Ma, D.-L.; Wong, K.-Y.; Tang, J. C.-O.; Chan, A. S.-C.; Gu, L.-Q. Stabilization of G-quadruplex DNA and down-regulation of oncogene c-myc by quindoline derivatives. *J. Med. Chem.* **2007**, *50*, 1465–1474. (b) Tan, J.-H.; Ou, T.-M.; Hou, J.-Q.; Lu, Y.-J.; Huang, S.-L.; Luo, H.-B.; Wu, J.-Y.; Huang, Z.-S.; Wong, K.-Y.; Gu, L.-Q. Isaindigotone derivatives: a new class of highly selective ligands for telomeric G-quadruplex DNA. *J. Med. Chem.* **2009**, *52*, 2825–2835. (c) Li, J.; Jin, X.; Hu, L.; Wang, J.; Su, Z. Identification of nonplanar small molecule for G-quadruplex grooves: molecular docking and molecular dynamic study. *Bioorg. Med. Chem. Lett.* **2011**, *21*, 6969–6972.
- (16) Georgiades, S. N.; Karim, N. H. A.; Suntharalingam, K.; Vilar, R. Interaction of metal complexes with G-quadruplex DNA. *Angew. Chem., Int. Ed.* **2010**, *49*, 4020–4034.
- (17) (a) Reed, J. E.; Arnal, A. A.; Neidle, S.; Vilar, R. Stabilization of G-quadruplex DNA and inhibition of telomerase activity by square-planar nickel(II) complexes. *J. Am. Chem. Soc.* **2006**, *128*, 5992–5993. (b) Zhao, C.; Ren, J.; Xu, Y.; Qu, X. Targeting human telomeric higher-order DNA: dimeric G-quadruplex units serve as preferred binding site. *J. Am. Chem. Soc.* **2013**, *135*, 18786–18789.
- (18) (a) Kielytyka, R.; Fakhoury, J.; Moitessier, N.; Sleiman, H. F. Platinum phenanthroimidazole complexes as G-quadruplex DNA selective binders. *Chem.—Eur. J.* **2008**, *14*, 1145–1154. (b) De Cian, A.; DeLemos, E.; Mergny, J.-L.; Teulade-Fichou, M.-P.; Monchaud, D. Highly efficient G-quadruplex recognition by bisquinolinium compounds. *J. Am. Chem. Soc.* **2007**, *129*, 1856–1857. (c) Reed, J. E.; Neidle, S.; Vilar, R. Stabilisation of human telomeric quadruplex DNA and inhibition of telomerase by a platinum-phenanthroline complex. *Chem. Commun.* **2007**, *42*, 4366–4368. (d) Kielytyka, R.; Englebienne, P.; Fakhoury, J.; Autexier, C.; Moitessier, N.; Sleiman, H. F. A platinum supramolecular square as an effective G-quadruplex binder and telomerase inhibitor. *J. Am. Chem. Soc.* **2008**, *130*, 10040–10041. (e) Ma, D.-L.; Che, C.-M.; Yan, S.-C. Platinum(II) complexes with dipyrrophenazine ligands as human telomerase inhibitors and luminescent probes for G-quadruplex DNA. *J. Am. Chem. Soc.* **2009**, *131*, 1835–1846. (f) Choudhury, J. R.; Guddneppanavar, R.; Saluta, G.; Kucera, G. L.; Bierbach, U. Tuning the DNA conformational perturbations inducing by cytotoxic platinum-acridine bisintercalators: effect of metal cis/trans isomerism and DNA threading groups. *J. Med. Chem.* **2008**, *51*, 3069–3072. (g) Zhu, J.; Zhao, Y.; Zhu, Y.; Wu, Z.; Lin, M.; He, W.; Wang, Y.; Chen, G.; Dong, L.; Zhang, J.; Lu, Y.; Guo, Z. DNA cross-linking patterns induced by an antitumor-active trinuclear platinum complexes and comparison with its dinuclear analogue. *Chem.—Eur. J.* **2009**, *15*, 5245–5253.
- (19) (a) Zheng, X.-H.; Chen, H.-Y.; Tong, M.-L.; Ji, L.-N.; Mao, Z.-W. Platinum squares with high selectivity and affinity for human telomeric G-quadruplexes. *Chem. Commun.* **2012**, *48*, 7607–7607. (b) Zheng, X.-H.; Zhong, Y.-F.; Tan, C.-P.; Ji, L.-N.; Mao, Z.-W. Pt(II) squares as selective and effective human telomeric G-quadruplex

- binders and potential cancer therapeutics. *Dalton Trans.* **2012**, *42*, 11807–11812. (c) Viglasky, V. Platination of telomeric sequences and nuclease hypersensitive elements of human-c-myc and PDGF-A promoters and their ability to form G-quadruplexes. *FEBS J.* **2009**, *276*, 401–409. (d) Wang, J.; Lu, K.; Xuan, S.; Toh, Z.; Zhang, D.; Shao, F. A Pt(II)-Dip complex stabilizes parallel c-myc G-quadruplex. *Chem. Commun.* **2013**, *49*, 4758–4760. (e) Bertrand, H.; Bombard, S.; Monchaud, D.; Teulade-Fichou, M.-P. A platinum-quinacridine hybrid as a G-quadruplex ligand. *J. Biol. Inorg. Chem.* **2007**, *12*, 1003–1014. (f) Colangelo, D.; Ghiglia, A. L.; Viano, L.; Cavigliolo, G.; Osella, D. Cis-[Pt(Cl)₂(pyridine)(5-SO₃H-isoquinoline) complex, as selective inhibitor of telomerase enzyme. *BioMetals* **2003**, *16*, 553–560. (g) Bombard, S.; Gariboldi, M. B.; Monti, E.; Gabano, E.; Gaviglio, L.; Ravera, M.; Osella, D. Biological activity of enantiomeric complexes [PtCIL] (L is aromatic bisphosphanes and aromatic diamines). *J. Biol. Inorg. Chem.* **2010**, *15*, 841–850.
- (20) Largy, E.; Hamon, F.; Rosu, F.; Gabelica, V.; Pauw, E. D.; Guedin, A.; Mergny, J.-L.; Teulade-Fichou, M.-P. Tridentate N-donor palladium(II) complexes as efficient coordinating quadruplex DNA binders. *Chem.—Eur. J.* **2011**, *17*, 13274–13283.
- (21) (a) Shi, S.; Gao, S.; Cao, T.; Liu, J.; Gao, X.; Hao, J.; Lv, C.; Huang, H.; Xu, J.; Yao, T. Targeting human telomeric G-quadruplex DNA and inhibition of telomerase activity with [(dmb)₂Ru(obip)Ru(dmb)₂]⁴⁺. *PLoS One* **2013**, *8*, e84419. (b) Li, Q.; Zhang, J.; Yang, L.; Yu, Q.; Chen, Q.; Qin, X.; Le, F.; Zhang, Q.; Liu, J. Stabilization of G-quadruplex DNA and inhibition of telomerase activity of ruthenium(II) complexes. *J. Inorg. Biochem.* **2014**, *130*, 122–129. (c) Zhang, J.; Yu, Q.; Li, Q.; Yang, L.; Chen, L.; Zhou, Y.; Liu, J. A ruthenium(II) complex capable of inducing and stabilizing bcl-2 G-quadruplex formation as a potential cancer inhibitor. *J. Inorg. Biochem.* **2014**, *134*, 1–11. (d) Wang, C.; Yu, Q.; Yang, L.; Liu, Y.; Sun, D.; Huang, Y.; Zhou, Y.; Zhang, Q.; Liu, J. Ruthenium(II) polypyridyl complexes stabilize the bcl-2 promoter quadruplex and induce apoptosis of HeLa tumor cells. *BioMetals* **2013**, *26*, 387–402.
- (22) Li, M.-J.; Lan, T.-Y.; Lin, Z.-S.; Yi, C.; Chen, G.-N. Synthesis, characterization, and DNA binding of a novel ligand and its Cu(II) complex. *J. Biol. Inorg. Chem.* **2013**, *18*, 993–1003.
- (23) Von, S.-T.; Seng, H.-L.; Lee, H.-B.; Ng, S.-W.; Kitamura, Y.; Chikira, M.; Ng, C.-H. DNA molecular recognition and cellular selectivity of anticancer metal(II) complexes of ethylenediamineacetate and phenanthroline: multiple targets. *J. Biol. Inorg. Chem.* **2012**, *17*, 57–69.
- (24) Tang, H.; Wang, X.-D.; Wei, Y.-B.; Huang, S.-L.; Huang, Z.-S.; Tan, J.-H.; An, L.-K.; Wu, J.-Y.; Chan, A. S.-C.; Gu, L.-Q. Oxoisoporphine alkaloid derivatives: synthesis, DNA binding affinity and cytotoxicity. *Eur. J. Med. Chem.* **2008**, *43*, 973–980.
- (25) Tang, H.; Zhao, H.-T.; Zhong, S.-M.; Wang, Z.-Y.; Chen, Z.-F.; Liang, H. Novel oxoisoporphine-based inhibitors of acetyl- and butyrylcholinesterase and acetylcholinesterase-induced beta-amyloid aggregation. *Bioorg. Med. Chem. Lett.* **2012**, *22*, 2257–2261.
- (26) Schreiber, E.; Matthias, P.; Mueller, M. M.; Schaffner, W. Rapid detection of octamer binding proteins with “mini-extracts” prepared from a small number of cells. *Nucleic Acids Res.* **1989**, *17*, 6419.
- (27) Zawada, W. M.; Kirschman, D. L.; Cohen, J. J.; Heidenreich, K. A.; Freed, C. R. *Exp. Neurol.* **1996**, *140*, 60–67.
- (28) (a) Cosconati, S.; Rizzo, A.; Trotta, R.; Pagano, B.; Iachettini, S.; De Tito, S.; Lauri, L.; Fotticchia, I.; Giustiniano, M.; Marinelli, L.; Giancola, C.; Novellino, E.; Biroccio, A.; Randazzo, A. Shooting for selective druglike G-quadruplex binders: evidence for telomeric DNA damage and tumor cell death. *J. Med. Chem.* **2012**, *55*, 9785–9792. (b) Burger, A. M.; Dai, F.; Schultes, C. M.; Reszka, A. P.; Moore, M. J.; Double, J. A.; Neidle, S. The G-quadruplex-interactive molecule BRACO-19 inhibits tumor growth, consistent with telomere targeting and interference with telomerase function. *Cancer Res.* **2005**, *65*, 1489–1496. (c) Ou, T.-M.; Lin, J.; Lu, Y.-J.; Hou, J.-Q.; Tan, J.-H.; Chen, S.-H.; Li, Z.; Li, Y.-P.; Li, D.; Gu, L.-Q.; Huang, Z.-S. Inhibition of cell proliferation by quindoline derivative (SYUIQ-05) through its preferential interaction with c-myc promoter G-quadruplex. *J. Med. Chem.* **2011**, *54*, 9671–9679.
- (29) (a) Chong, L.; van Steensel, B.; Broccoli, D.; Erdjument-Bromage, H.; Hanish, J.; Tempst, P.; de Lange, T. A human telomeric protein. *Science* **1995**, *270* (5242), 1663–1667. (b) Broccoli, D.; Smogorzewska, A.; Chong, L.; de Lange, T. Human telomeres contain two distinct Myb-related proteins, TRF1 and TRF2. *Nat. Genet.* **1997**, *17* (2), 231–235.
- (30) van Steensel, B.; de Lange, T. Control of telomere length by the human telomeric protein TRF1. *Nature* **1997**, *385*, 740–743.
- (31) Bilaud, T.; Brun, C.; Ancelin, K.; Koering, C. E.; Laroche, T.; Gilson, E. Telomeric localization of TRF2, a novel human telobox protein. *Nat. Genet.* **1997**, *17*, 236–239.
- (32) Smogorzewska, A.; van Steensel, B.; Bianchi, A.; Oelmann, S.; Schaefer, M. R.; Schnapp, G.; de Lange, T. Control of human telomere length by TRF1 and TRF2. *Mol. Cell. Biol.* **2000**, *20*, 1659–1668.
- (33) (a) Takai, H.; Smogorzewska, A.; de Lange, T. DNA damage foci at dysfunctional telomeres. *Curr. Biol.* **2003**, *13*, 1549–1556. (b) Celli, G. B.; de Lange, T. DNA processing is not required for ATM mediated telomere damage response after TRF2 deletion. *Nat. Cell Biol.* **2005**, *7*, 712–718. (c) Fradet-Turcotte, A.; Canny, M. D.; Escribano-Diaz, C.; Orthwein, A.; Leung, C. C. Y.; Huang, H.; Landry, M.-C.; Kitevski-LeBlanc, J.; Noordermeer, S. M.; Sicheri, F.; Durocher, D. 53BP1 is a reader of the DNA-damage-induced H2A Lys 15 ubiquitin mark. *Nature* **2013**, *499* (7456), 50–54. (d) Smogorzewska, A.; van Steensel, B.; Bianchi, A.; Oelmann, S.; Schaefer, M. R.; Schnapp, G.; de Lange, T. Control of human telomere length by TRF1 and TRF2. *Mol. Cell. Biol.* **2000**, *20* (5), 1659–1668.
- (34) Stroth, C.; Schulze-Osthoff, K. Death by a thousand cuts: an ever increasing list of caspase substrates. *Cell Death Differ.* **1998**, *5*, 997–1000.
- (35) (a) Monchaud, D.; Allain, C.; Bertrand, H.; Smargiasso, N.; Rosu, F.; Gabelica, V.; De Cian, A.; Mergny, J.-L.; Teulade-Fichou, M.-P. Ligands playing musical chairs with G-quadruplex DNA: a rapid and simple displacement assay for identifying selective G-quadruplex binders. *Biochimie* **2008**, *90* (8), 1207–1223. (b) Xu, Y. Chemistry in human telomere biology: structure, function and targeting of telomere DNA/RNA. *Chem. Soc. Rev.* **2011**, *40*, 2719–2740. (c) Xu, Y.; Ishizuka, T.; Kurabayashi, K.; Komiyama, M. Consecutive formation of G-quadruplexes in human telomeric-overhang DNA: a protective capping structure for telomere ends. *Angew. Chem., Int. Ed.* **2009**, *48*, 7833–7836. (d) Wang, X.-D.; Ou, T.-M.; Lu, Y.-J.; Li, Z.; Xu, Z.; Xi, C.; Tan, J.-H.; Huang, S.-L.; An, L.-K.; Li, D.; Gu, L.-Q.; Huang, Z.-S. Turning off transcription of the bcl-2 gene by stabilizing the bcl-2 promoter quadruplex with quindoline derivatives. *J. Med. Chem.* **2010**, *53*, 4390–4398. (e) Seenisamy, J.; Rezler, E. M.; Powell, T. J.; Tye, D.; Gokhale, V.; Joshi, C. S.; Siddiqui-Jain, A.; Hurley, L. H. The dynamic character of the G-quadruplex element in the c-MYC promoter and modification by TMPyP4. *J. Am. Chem. Soc.* **2004**, *126*, 8702–8709. (f) Yuan, L.; Tian, T.; Chen, Y.; Yan, S.; Xing, X.; Zhang, Z.; Zhai, Q.; Xu, L.; Wang, S.; Weng, X.; Yuan, B.; Zhou, X. Existence of G-quadruplex structures in promoter region of oncogenes confirmed by G-quadruplex DNA cross-linking strategy. *Sci. Rep.* **2013**, DOI: 10.1038/srep01811. (g) Zhu, J.; Zhao, Y.; Zhu, Y.; Wu, Z.; Lin, M.; He, W.; Wang, Y.; Chen, G.; Dong, L.; Zhang, J.; Lu, Y.; Guo, Z. DNA cross-linking patterns induced by an antitumor-active trinuclear platinum complex and comparison with its dinuclear analogue. *Chem.—Eur. J.* **2009**, *15*, 5245–5253.
- (36) (a) Andrews, P. A.; Murphy, M. P.; Howell, S. B. Metallothionein-mediated cisplatin resistance in human ovarian carcinoma cells. *Cancer Chemother. Pharmacol.* **1987**, *19*, 149–154. (b) Kang, Y. J.; Enger, M. D.; Naidenova, E.; Ivanov, E.; Adzharov, D. Glutathione is involved in the early cadmium cytotoxic response in human lung carcinoma cells. *Toxicology* **1988**, *48*, 93–101. (c) Ochi, T.; Otsuka, F.; Takahashi, K.; Ohsawa, M. Glutathione and metallothioneins as cellular defense against cadmium toxicity in cultured Chinese hamster cells. *Chem.-Biol. Interact.* **1988**, *65*, 1–14. (d) Connors, D. E.; Ringwood, A. H. Effects of glutathione depletion on copper cytotoxicity in oysters (*Crassostrea virginica*). *Aquat. Toxicol.* **2000**, *50*, 341–349.

- (37) (a) Zelazowski, A. J.; Garvey, J. S.; Hoeschele, J. D. The in vivo and in vitro binding of platinum to metallothionein. *Arch. Biochem. Biophys.* **1984**, *229*, 246–252. (b) Knipp, M. Metallothioneins and platinum(II) anti-tumor compounds. *Curr. Med. Chem.* **2009**, *16*, 522–537. (c) Kelland, L. The resurgence of platinum-based cancer chemotherapy. *Nat. Rev. Cancer* **2007**, *7*, 573–584.
- (38) Postel, E. H.; Berberich, S. J.; Flint, S. J.; Ferrone, C. A. Human c-myc transcription factor PuF identified as nm23-2 nucleoside diphosphate kinase, a candidate suppressor of tumor metastasis. *Science* **1993**, *261*, 478–480.
- (39) (a) Kyo, S.; Takakura, M.; Taira, T.; Kanaya, T.; Itoh, H.; Yutsudo, M.; Ariga, H.; Inoue, M. Sp1 cooperates with c-myc to activate transcription of the human telomerase reverse transcriptase gene (hTERT). *Nucleic Acids Res.* **2000**, *28*, 669–677. (b) Wu, K.-J.; Grandori, C.; Amacker, M.; Simon-Vermot, N.; Polack, A.; Lingner, J.; Dalla-Favera, R. Direct activation of TERT transcription by c-MYC. *Nat. Genet.* **1999**, *21*, 220–224. (c) Gunes, C.; Lichtsteiner, S.; Vasserot, A. P.; Englert, C. Expression of the hTERT gene is regulated at the level of transcriptional initiation and repressed by mad1. *Cancer Res.* **2000**, *60*, 2116–2121. (d) Greenberg, R. A.; O'Hagan, R. C.; Deng, H.; Xiao, Q.; Hann, S. R.; Adams, R. R.; Lichtsteiner, S.; Chin, L.; Morin, G. B.; DePinho, R. A. Telomerase reverse transcriptase gene is a direct target of c-Myc but is not functionally equivalent in cellular transformation. *Oncogene* **1999**, *18*, 1219–1226. (e) Ducrest, A.-L.; Amacker, M.; Mathieu, Y. D.; Cuthbert, A. P.; Trott, D. A.; Newbold, R. F.; Nabholz, M.; Lingner, J. Regulation of human telomerase activity: repression by normal chromosome 3 abolishes nuclear telomerase reverse transcriptase transcripts but does not affect c-Myc activity. *Cancer Res.* **2001**, *61*, 7594–7602. (f) Wang, J.; Xie, L. Y.; Allan, S. Myc activates telomerase. *Genes Dev.* **1998**, *12*, 1769–1774.
- (40) Wu, K.-J.; Grandori, C.; Amacker, M.; Simon-Vermot, N.; Polack, A.; Lingner, J.; Dalla-Favera, R. Direct activation of TERT transcription by c-MYC. *Nat. Genet.* **1999**, *21*, 220–224.
- (41) Chalfie, M.; Tu, Y.; Euskirchen, G.; Ward, W. W.; Prasher, D. C. Green fluorescent protein as a marker for gene expression. *Science* **1994**, *263*, 802–805.
- (42) He, T.-C.; Sparks, A. B.; Rago, C.; Hermeking, H.; Zawel, L.; Da Costa, L. T.; Morin, P. J.; Vogelstein, B.; Kinzler, K. W. Identification of c-MYC as a target of the APC pathway. *Science* **1998**, *281*, 1509–1512.
- (43) Redon, S.; Reichenbach, P.; Lingner, J. The non-coding RNA TERRA is a natural ligand and direct inhibitor of human telomerase. *Nucleic Acids Res.* **2010**, *38*, 5797–5806.
- (44) (a) Tauchi, T.; Shin-ya, K.; Sashida, G.; Sumi, M.; Okabe, S.; Ohyashiki, J. H.; Ohyashiki, K. Telomerase inhibition with a novel G-quadruplex-interactive agent, telomestatin: in vitro and in vivo studies in acute leukemia. *Oncogene* **2006**, *25*, 5719–5725. (b) Zhou, J.-L.; Lu, Y.-J.; Ou, T.-M.; Zhou, J.-M.; Huang, Z.-S.; Zhu, X.-F.; Du, C.-J.; Bu, X.-Z.; Ma, L.; Gu, L.-Q.; Li, Y.-M.; Chan, A. S.-C. Synthesis and evaluation of quindoline derivatives as G-quadruplex inducing and stabilizing ligands and potential inhibitors of telomerase. *J. Med. Chem.* **2005**, *48*, 7315–7321.
- (45) Kim, N. W.; Piatyszek, M. A.; Prowse, K. R.; Harley, C. B.; West, M. D.; Ho, P. L.; Coviello, G. M.; Wright, W. E.; Weinrich, S. L.; Shay, J. W. Specific association of human telomerase activity with immortal cells and cancer. *Science* **1994**, *266*, 2011–2015.
- (46) Samari, F.; Hemmateejad, B.; Shamsipur, M.; Rashidi, M.; Samouei, H. Affinity of two novel five-coordinated anticancer Pt(II) complexes to human and bovine serum albumins: a spectroscopic approach. *Inorg. Chem.* **2012**, *51*, 3454–3464.
- (47) Raja, D. S.; Bhuvanesh, N. S. P.; Natarajan, K. Biological evaluation of a novel water soluble sulphur bridged binuclear copper(II) thiosemicarbazone complex. *Eur. J. Med. Chem.* **2011**, *46*, 4584–4594.
- (48) Grant, T.; Bennett-Wood, V.; Robins-Browne, R. M. Characterization of the interaction between *Yersinia enterocolitica* biotype 1A and phagocytes and epithelial cells in vitro. *Infect. Immun.* **1999**, *67*, 4367–4375.
- (49) Wang, P.; Leung, C.-H.; Ma, D.-L.; Yan, S.-C.; Che, C.-M. Structure-based design of platinum(II) complexes as c-myc oncogene down-regulators and luminescent probes for G-quadruplex DNA. *Chem.—Eur. J.* **2010**, *16*, 6900–6911.
- (50) (a) Sheldrick, G. M. *SHELXTL-97, Program for Refinement of Crystal Structures*; University of Göttingen: Göttingen, Germany, 1997. (b) Sheldrick, G. M. *SHELXS-97, Program for Solution of Crystal Structures*; University of Göttingen: Göttingen, Germany, 1997.
- (51) Biroccio, A.; Benassi, B.; Filomeni, G.; Amodei, S.; Marchini, S.; Chiorino, G.; Rotilio, G.; Zupi, G.; Ciriolo, M. R. Glutathione in fluences c-Myc-induced apoptosis in M14 human melanoma cells. *J. Biol. Chem.* **2002**, *277*, 43763–43770.
- (52) Wang, Y.-Q.; Zhang, H.-M.; Zhang, G.-C.; Tao, W.-H.; Tang, S.-H. Interaction of the flavonoid hesperidin with bovine serum albumin: a fluorescence quenching study. *J. Lumin.* **2007**, *126*, 211–218.
- (53) Yang, H.; Ou, C. C.; Feldman, R. I.; Nicosia, S. V.; Kruk, P. A.; Cheng, J. Q. Aurora-A kinase regulates telomerase activity through c-Myc in human ovarian and breast epithelial cells. *Cancer Res.* **2004**, *64*, 463–467.
- (54) Sun, J.; Blaskovich, M.; Knowles, D.; Qian, Y.; Ohkanda, J.; Bailey, R.; Hamilton, A.; Sebt, S. Antitumor efficacy of a novel class of nonthiol-containing peptidomimetic inhibitors of farnesyltransferase and geranylgeranyltransferase I. *Cancer Res.* **1999**, *59*, 4919–4926.
- (55) Palanimuthu, D.; Shinde, S. V.; Somasundaram, K.; Samuelson, A. G. In vitro and in vivo anticancer activity of copper bis-(thiosemicarbazone) complexes. *J. Med. Chem.* **2013**, *56*, 722–734.